Origin of volcanic-hosted Mn-oxide mineralization from San Pietro Island (SW Sardinia, Italy): an integrated geochemical, mineralogical and isotopic study

Pitzalis E. [1], Fulignati P.[1,*], Lezzerini M.[1], Cioni R.[2], Pinarelli L.[3], Tamponi M.[1], Gioncada A.[1]

[1]Department of Earth Sciences, University of Pisa, via S. Maria 53, 56126 Pisa, Italy

[2]Department of Earth Sciences, University of Florence, via La Pira 4, 50121 Firenze, Italy

[3]Institute of Geosciences and Earth Resources, Section of Florence, National Research Council (CNR), via La Pira 4, 50121 Florence, Italy

*Corresponding author: Paolo Fulignati (paolo.fulignati@unipi.it)

Highlights

We studied volcanic-hosted Mn-oxide ores of San Pietro Island (Italy)

An integrated geochemical, mineralogical and isotopic study was undertaken

We discuss San Pietro ores based on trace element discrimination schemes for Mn ores

The physical and chemical conditions of Mn transport and precipitation are assessed

A mixed low-T hydrothermal-hydrogenetic model is proposed

Abstract

The Mn-oxide mineralizations from Sardinia (Italy) represent examples of Mn deposits in a continental environment and, as such, their investigation can shed light on the genesis and characteristics of this deposit type, less studied than their more common oceanic counterpart. In this paper, the genetic mechanisms, the physical-chemical conditions and the origin of the mineralizing fluids are discussed for the volcanic-hosted Mn ores of the San Pietro Island (SW Sardinia), through an integrated geochemical, mineralogical and radiogenic isotope approach. New and published data are here examined on the basis of recent trace element discrimination schemes for Mn ores and a model for the genesis is proposed.

The mineralogy of the alteration paragenesis (argillic facies) and the type of observed fluid inclusions (very small monophase liquid inclusions) suggest a circulation of mineralizing fluids characterized by weak acidic conditions (pH indicatively around 5) and relatively low temperature (<100-120°C). Geochemical features such as the contents of transition metals (Mn, Fe, Cu, Co, Ni, Zn), and contents and ratios of rare-earth elements and yttrium (REY), suggest that the San Pietro Island Mn metallogenesis is the result of combined hydrothermal and hydrogenetic mechanisms of formation. The Pb isotope compositions of different Mn veins exhibit a significant spread that suggests the contribution of distinct mineralizing fluids, deriving their isotopic signature from both seawater and water-rock interaction processes.

The possible model of formation of the San Pietro Mn mineralization can be viewed as a complex process, in which Mn-bearing fluids originated from remobilization of Mn oxides sequestered in shelf and slope sediments and/or by leaching of the older Cenozoic volcanic rocks that form the basement of the island. Fluid rise was due to hydrothermal convection, possibly related to the general thermal anomaly active in the area from 15 to 12 My, during the final stage of the intense Cenozoic volcanic activity of the Sulcis area (San Pietro, Sant'Antioco, Isola del Toro volcanic activity). The fluids were probably dominated by seawater, characterized by relatively low temperatures and acidic conditions, due to the input of H_2S of hydrothermal origin. The Mn ore

47 deposition occurred in relatively shallow water and oxidizing environment, following the pH
48 neutralization induced by water-rock interaction processes.

49

50 **Keywords:** Mn-ore; volcanic-hosted; mineralizing fluids; REE; Pb isotopes, Sardinia.

51

52 **1. Introduction**

53 Since prehistoric times, Sardinia Island (Italy) has been the locus of an intense mining activity. The
54 large variety of its deposits spans from the relevant polymetallic Pb-Zn hydrothermal (SEDEX,
55 Mississippi-Valley-type) to epithermal (low and high sulfidation) mineralization to polymetallic
56 skarns, and include raw materials for ceramic and glass industries, ornamental stones, coal and
57 bauxite mines (e.g., Boni et al., 1996; Ruggieri et al., 1997; Palomba et al., 2006). Important Mn
58 oxide mineralization, also, occur in the northwestern and southwestern portions of the island
59 (Guerin, 1983; Sinisi et al., 2012). These Mn deposits include both sediment-hosted (Mt. Jorzi,
60 Ittiri-Uri, Padria areas - NW Sardinia) and volcanic-hosted (Anglona area - NW Sardinia and San
61 Pietro Island - SW Sardinia) types, interpreted by previous studies as diagenetic and hydrothermal
62 (mixing of magmatic and meteoric waters) respectively (Sinisi et al., 2012; Mongelli et al., 2013).
63 The Sardinian deposits are associated to a continental arc environment (Sinisi et al., 2012). While
64 genetic mechanisms of Mn-ore in the oceanic environment are relatively well constrained (e.g.
65 Nicholson, 1992; Xiao et al., 2017), few studies exist regarding the genesis of Mn mineralizations
66 in the shallow marine/continental environment. In order to shed some light on the possible
67 processes related to these deposits, this paper deals with the volcanic-hosted Mn-ores of the San
68 Pietro Island, located in the southwestern part of Sardinia.

69 Here we applied an integrated geochemical, mineralogical and radiogenic isotope approach and
70 used both new and available data from literature (Sinisi et al., 2012) to propose a constrained ore-
71 forming model for Mn-oxide ores at San Pietro Island. In particular, geochemistry of rare-earth

elements (REE), recent trace element discrimination schemes for Mn ores (Bau et al., 2014; Josso et al., 2017), Pb isotope systematics, and mineralogy are employed to characterize the origin of the mineralizing fluids responsible of Mn-ore formation, and to trace the ore forming processes.

2. Geological setting

During the last 30 Ma, the Alpine orogenesis deeply controlled the geological evolution of the entire circum-Mediterranean area, including the Sardinia-Corsica block. During upper Oligocene-lower Miocene, the NNW-trending subduction of African oceanic lithosphere below the margin of the European continental plate triggered the opening of the Ligurian-Provençal back-arc basin (Beccaluva et al., 1994; Catalano et al., 2001; Speranza et al., 2002), thus starting the counter-clockwise rotation of the Sardinia-Corsica block, which definitively stopped in Langhian times (around 15 Ma) (Speranza et al., 2002).

Regional geodynamics culminated in two distinct igneous episodes (Oligo-Miocene and Plio-Quaternary), with a varied magmatic activity ranging in composition from subalkaline to strongly alkaline (Lustrino et al., 2004; 2013). The Oligo-Miocene volcanic activity (32-15 Ma) was linked to the development of a magmatic arc along the western margin of the Sardinia-Corsica microplate. The volcanic products (dacitic to rhyolitic ignimbrites with a subalkaline affinity) are mainly distributed over the central-western sector of the island along the "Fossa Sarda", a N-S to NW-SE graben-like structure that crosses Sardinia from North to South. The climax of the volcanic activity occurred between 23 and 18 Ma, during the period of maximum extension of the Ligurian-Provençal basin (Lustrino et al., 2013).

The Sulcis Volcanic Province (SVP), located at the southwestern margin of Sardinia (Boni et al., 1990; Morra et al., 1994; Cioni et al., 2001), represents the last manifestations of the Oligo-Miocene igneous phase (Lustrino et al., 2013). This province includes the Sant'Antioco and San Pietro Islands and part of the Sulcis mainland. According to Morra et al. (1994), the SVP is

97 characterized by two phases: an *Old Phase* (28.4-17.7 Ma) dominated by basaltic to intermediate
98 lavas with subordinate pyroclastic products having calc-alcaline affinity and outcropping in the
99 Sulcis mainland and in the Sant' Antioco Island; and a *Young Phase* (17.6-13.8 Ma), characterized
100 by at least 11 main ignimbrite sheets ranging from trachytes to rhyolites in composition, with calc-
101 alcaline to peralkaline affinity, that crop out in the Sulcis mainland and in Sant'Antioco and San
102 Pietro Islands (Boni et al., 1990; Cioni et al., 2001; Mundula et al., 2009; Fig. 1A).

103 San Pietro is an island completely formed by volcanic terrains emplaced during the most
104 recent portion of the *Young Phase* (Fig. 1A). Peralkaline, mainly comenditic, lava flows and
105 ignimbrites extensively crop out in the northern part of the island, where some vents related to the
106 effusive activity of this phase are also present (Araña et al., 1974; Garbarino et al., 1990). These
107 peralkaline products are interlayered within the products of the calc-alkaline activity (Fig. 1B). All
108 the volcanic products were subaerially emplaced within a time span of about 1 Ma starting from
109 15.8 Ma (Pioli and Rosi, 2005). Disseminated Mn-ores are present in some of the main units, being
110 especially present in the peralkaline units (both lava flows and ignimbrites) or at the contact
111 between these and the interlayered calc-alkaline units (Garbarino et al., 1990).

112

113 *2.1 Mn mineralization of San Pietro Island*

114 The Mn-ore deposits of San Pietro Island are part of the Sulcis-Iglesiente mining district.
115 Based on available published data (Uras, 1965), the orebodies were roughly estimated to contain
116 400,000 tons of Mn ores, with a grade in the range of 5-40 wt% as Mn. The mineralization form
117 irregular masses and vein swarms in the volcanic units. The largest deposit is, instead, a stratiform
118 orebody of 4-8 m of thickness, intercalated with ochres and opal and quartz in a volcano-
119 sedimentary environment (Guerin, 1973; Garbarino et al., 1990; Sinisi et al., 2012). Some of the Mn
120 deposits of the San Pietro Island were considered economically exploitable in the past. This is the
121 case of *Cala Fico*, *La Piramide*, *Capo Becco-Capo Rosso*, *Punta Nera-Le Lille* mines (Fig. 1A),

where Mn ores were mined, with a fluctuating trend, throughout the last century until the 1970s when the mining activity definitively ended.

3. Analytical methods

Polished thin sections of the Mn-oxide veins and host rock were studied by means of reflected and transmitted light microscopy. The thin sections, as well as Mn-ore fragments, were carbon-coated and analyzed by SEM-BSEI (scanning electron microscope and back-scattered electrons imaging) and EDS (energy-dispersion spectroscopy) with a Philips XL30, equipped with an Edax Genesis microanalytical device (20 kV filament voltage, 10 mm working distance, up to 5,000 magnifications) at the Department of Earth Sciences, University of Pisa, and by FE-SEM (field emission scanning electron microscope) and EDS with a FEI Quanta 450 equipped with a Bruker microanalytical system (20 kV filament voltage, 10 mm working distance, up to 60,000 magnifications) at the Centro Interdipartimentale di Scienza e Ingegneria dei Materiali, University of Pisa.

The samples from the Mn veins were crushed and the Mn ore manually separated from the host rock. Samples representative of the host rocks (lava and ignimbrites) were also crushed and visually cleaned of any Mn-ore impurities. In the case of ignimbrites, samples are representative of both the juvenile fraction (coarse juvenile clasts) and the bulk ignimbrite rock. The separated ore and host rock were finely powdered with agate ball mills.

The chemical composition of selected samples was determined by X-ray Fluorescence (XRF) on pressed powder pellets using an ARL 9400 XP+ sequential X-ray spectrometer under the instrumental conditions reported in Lezzerini et al. (2013). Within the range of the measured concentrations, the analytical uncertainties are <5% for all the components except for Na_2O, Al_2O_3, SiO_2, K_2O and MnO, which may occasionally attain <10% for very low concentrations (Lezzerini et

146 al., 2013, 2014). The total amount of volatile components was determined as loss on ignition (LOI
147 in 105-950°C temperature range).

148 Trace-element analyses of veins and host rock were carried out with an inductively coupled
149 plasma–mass spectrometer (ICP-MS; Perkin-Elmer NexION 300x) after sample digestion with aqua
150 regia + HF at Department of Earth Sciences, University of Pisa. Accuracy is within ±5%. Analysis
151 of REE concentrations was duplicated for two vein samples at ALS Chemex laboratories, by ICP-
152 MS after lithium metaborate fusion.

153 Pb isotope ratios were determined at the Institute of Geosciences and Earth Resources
154 (CNR) of Pisa using a Neptune MC-ICP-MS (Thermo Fisher Scientific Inc., Bremen, Germany).
155 Lead was analyzed after HF-HNO_3 dissolution of 50-200 mg of sample, followed by standard ion-
156 exchange chromatographic techniques. A thallium solution was added to both the sample and the
157 standard to correct for instrumental mass fractionation. The dilute nitric acid solutions were injected
158 into the mass spectrometer as aerosol through a quartz spray chamber. Only seven of the nine
159 Faraday cup collectors of the Neptune MS were used in the measurement of Pb isotope ratios in
160 static mode. Mercury was monitored for the correction of isobaric interference with ^{204}Pb, yet the
161 signal of ^{202}Hg was four orders of magnitude smaller than that of ^{204}Pb in the measurement of
162 sample solutions, so the effect of this interference was negligible as a matter of fact. Values used for
163 mass bias fractionation corrections were ^{205}Tl/^{203}Tl=2.388. Measured values were compared with
164 the international standard NBS981: ^{208}Pb/^{204}Pb=36.7007, ^{207}Pb/^{204}Pb=15.4891, ^{206}Pb/^{204}Pb=16.9656
165 (Todt et al., 1996). The reproducibility of the results of replicate analyses of the standard was
166 0.016–0.018% for the ^{206}Pb/^{204}Pb, ^{207}Pb/^{204}Pb, and ^{208}Pb/^{204}Pb ratios.

167 The qualitative mineralogical composition of bulk samples of both Mn ore and associated
168 altered host rock was obtained by X-ray powder diffraction analysis (XRPD). The diffraction
169 spectra were collected by an automatic diffractometer with Bragg-Brentano geometry, Bruker
170 model D2 PHASER 2nd Generation equipped with a Lynxeye 1D detector and Ni-filtered CuKα

171 radiation (λ=1.5406 Å). Data were scanned within the angular range 5-65 °2θ, with a step size of
172 0.02 °2θ and a counting time of 0.3 s/step. The Bruker AXS DIFFRAC.EVA software was used for
173 identifying the mineral phases.

174 XRPD analysis of the main phyllosilicates was carried out on one sample following the
175 procedures described by Moore & Reynolds (1997). XRPD patterns were recorded using a Philips
176 PW 1730 diffractometer with the following settings: CuK_{α} radiation obtained at 40 kV and 20 mA
177 and graphite monocromator; slits: 1° divergence and scatter, 0.2 mm receiving; scan speed:
178 1°2θ/min; step size of 0.2°θ and counting time of 2s per step. The clay mineral assemblage was
179 studied on Mg^{2+} and K^{+} saturated oriented mounts of the <2μm fraction. The Mg^{2+} saturated
180 specimens were measured in air-dried (AD) and glycolated (EG) states. K^{+} saturated mounts were
181 measured in air-dried conditions and after heating at 60, 300 and 550°C. The basal reflections of
182 clay minerals (including mixed-layer phases) were analyzed by the Brucker AXS DIFFRAC.EVA
183 suite for phase analysis.

184

185 **4. Results**

186 **4.1. Field reconnaissance**

187 Samples representative of the Mn ore and associated volcanic host rocks were collected
188 from the two abandoned mining sites of *La Piramide* (Il Macchione mine) and *Cala Fico*, located in
189 the central and north-western area of the San Pietro Island, respectively (Fig. 1A).

190 At *La Piramide*, the main Mn mineralization is particularly concentrated at the contact
191 between the Upper Comenditic Ignimbrite (UCI) and the overlying Monte Ulmus (MU) ignimbrite
192 (above, Fig. 1B, 2A). Mn varnishes characterize the ignimbrite outcrop close to the mine entrances.
193 The Mn ore consists of both individual centimeter-thickness veins and swarm veinlets (Fig. 2B).
194 Nodules were also observed. The Mn-oxide mineralization is also found as disseminated spots in

195 the host ignimbrite (O*celli* in Fig. 2C), showing a peculiar concentric texture. Locally, the
196 pyroclastics are completely altered into a powdery whitish mass, suggesting an argillification
197 process (Fig. 2D).

198 At *Cala Fico*, Mn oxide veins are widespread in a comenditic lava flow. The vein and
199 veinlet swarms are parallel to the main fractures and either parallel or crosscutting the pervasive
200 flow foliation of the rock (Fig. 2E). Locally, the ores occur also as patinae or crusts with a
201 botryoidal structure. Nodules are not observed at this site.

202

203 **4.2 Mineralogy and petrography**

204 From a petrographic and mineralogical point of view, the UCI and MU ignimbrites show
205 juvenile clasts with plurimillimetric quartz and alkali feldspar phenocrysts, and differ mainly for the
206 lower abundance of quartz phenocrysts of the latter. Rare mineral phases typical of peralkaline
207 products (aenigmatite, arfvedsonite, kaersutite, aegirine-augite) occur as microphenocrysts or in the
208 groundmass. In the La Piramide outcrops, the original volcanic glass is strongly altered and shows
209 spherulitic devitrification textures and zeolitization.

210 At *Cala Fico*, the porphyritic lava flow (phenocryst abundance of 25-30 % by volume), has
211 phenocrysts of quartz and alkali feldspar up to 5 mm, scarce kaersutite, aenigmatite and accessory
212 zircon and fayalite. The phenocrysts are hosted in a finely crystalline groundmass of quartz,
213 feldspars and rare arfvedsonite.

214 The Mn mineralization in the two sites is epigenetic; the veins consist of fracture filling
215 and/or of pervasive filling of the rock porosity by opaque Mn-bearing minerals. These show a
216 variable crystallinity, passing from a cryptocrystalline matrix to well-crystallized phases. Pervasive
217 filling is particularly evident in the highly porous ignimbritic lithologies at *La Piramide* (Figs. 3A,
218 B). Open space filling is demonstrated by the observed colloform and botryoidal textures, indicating
219 concentric overgrowths inward from vein walls (Fig. 3C), which in some cases leave incompletely

filled cavities. In the ignimbrites, the Mn minerals fill the space between tabular crystals of secondary zeolites, overgrown on the volcanic glass (Fig. 3C). Similarly, in the peculiar disseminated mineralization (*Ocelli*) found at *La Piramide*, the Mn minerals form small concretions between the crystals of the host rock and line up the open spaces in the host rock matrix (Figs. 4A, B, C, D).

Large volcanic quartz and K-feldspar phenocrysts can be easily recognized within the ore (Fig. 4E). In some cases, the quartz crystals host secondary fluid inclusions trails. The inclusions are very small in size (< 5 microns) and monophase (Fig. 5).

Mn opaque minerals represent almost the totality of the mineralization. Under reflected light, different opaque minerals can be recognized in polished thin sections, based on different reflectivity (Figs. 3A, B). This is confirmed by BSE images (Fig. 4D). EDS analyses carried out on the Mn minerals with different reflectivity revealed a K-rich Mn oxide and a Ba-rich one (Table 2). The Ba- and K-rich Mn oxides are in some cases intimately intermixed (Fig. 4D). In agreement with the petrographic and EDS data, XRPD results suggest the presence of two different Mn minerals, cryptomelane and hollandite, respectively the K-rich and Ba-rich phases, although minor pyrolusite cannot be excluded (Fig. 6A).

Secondary REE-bearing minerals (apatite, monazite, cerianite) are scattered in the Mn mineralization. The close association of REE anomalies with the Mn mineralization is also indicated by the sparse occurrence of Ce peaks in EDS spectra (probably revealing unresolvable micron-sized Ce-oxides) in the brightest regions of BSE images of the Mn-rich matrix (Cala Fico mineralization, Figs. 4 E, F).

Silica, barite and clays complete the ore paragenesis. Clays are dispersed with the pervasive mineralization and form the orange colored boundary visible at the margins of veins and nodules (Figs. 3D, 4G) both at La Piramide and Cala Fico. They are clearly associated to the Mn oxides, differently from other secondary minerals, probably zeolites (Fig. 4H), widespread in the ignimbrite

245 matrix at La Piramide and pre-dating the Mn oxides. XRPD analyses of clay minerals on oriented
246 mounts indicate smectite as the main mineralogical phase (Fig. 6B). Microanalytical EDS data
247 (Table 2) are well in agreement with XRPD data and show a limited compositional variation among
248 the analyzed smectites, which could be linked to the locally variable chemistry of the altered
249 materials (Fig. 7).

250 At *La Piramide*, in correspondence of the Mn orebody, a pervasive clay alteration affects the
251 pumice-bearing pyroclastics, resulting in a white-yellowish material with powdery appearance.
252 XRPD analysis shows the occurrence of kaolinite (Fig. 6C).

253

254 **4.3 Major and trace element geochemistry**

255 Major and trace element composition of both the mineralization (vein and disseminated
256 ores) and the host rock is reported in Table 1 and in the variation diagrams in Figure 8. Data from
257 Sinisi et al. (2012) for the same mining sites are also reported for comparison (VH2 and VH3
258 samples from La Piramide and Cala Fico, respectively). The rocks hosting the mineralization are
259 rhyolitic (Fig. 9), peralkaline or close to peralkalinity (Table 1). The composition of the veins is
260 enriched in MnO, Ba, Sr, Zr, U, Ni, Co and REE, but not in Fe_2O_3t, with respect to the rhyolite host
261 rocks (Fig. 8). For several elements, the samples from *Cala Fico* and those from *La Piramide* sites
262 plot in separate groups, showing distinct enrichment with respect to MnO content (Fig. 8). One
263 sample of *La Piramide* mineralization (QM-9o) falls very close to the host rocks in all diagrams
264 (Fig. 8). This sample represents the "Ocelli" Mn concretions and its chemical composition is
265 strongly affected by contamination from the host rock.

266

267 **4.3.1 REE geochemistry**

268 Rare earth elements contents of mineralization and host rocks are shown in Table 1. The
269 total REE content (ΣREE) of the mineralized samples displays a relatively wide range, from 276 to
270 4026 ppm, with an average value of 1740 ppm. These values are mostly well above those recorded
271 in the associated host rocks (average ΣREE value of 426 ppm with a maximum value of 558 ppm).
272 Remarkably, also the QM-9o sample ("Ocelli"), which shows clear evidences of strong
273 contamination by the host rock, results enriched in REE with respect to the host rock.

274 The chondrite-normalized distribution patterns of REE in the mineralized samples are
275 characterized by a significant fractionation between the LREE and the HREE, which is higher than
276 in the host rocks (Fig. 10). La/Lu ratios in Mn ore are indeed between 107 and 336 with an average
277 value of 189, whereas they vary from 34 to 88, with an average value of 62, in the host rocks.

278 In the mineralized samples, the values of $(Ce/Ce^*)_{CN}$ vary from 0.56 to 2.04, thus showing
279 either a positive (QM-6v, QM-14v) or negative (QM-2v, QM-8v) Ce anomaly (Fig. 10, Tab. 1). The
280 Eu anomaly, expressed as $(Eu/Eu^*)_{CN}$, is negative in all the analyzed samples. It varies from 0.02 to
281 0.28, with an average value of 0.15, in the mineralized samples. These values are slightly higher
282 than those shown by the host rocks (between 0.02 and 0.11, with an average value of 0.08).

283

284 **4.4 Pb isotope geochemistry**

285 The Pb isotope ratios of three samples of Mn-oxide veins, one from *Cala Fico* and two from
286 *La Piramide*, are reported in Table 1. The manganese mineralization of *Cala Fico* has $^{206}Pb/^{204}Pb$ =
287 18.749, $^{207}Pb/^{204}Pb$ = 15.665 and $^{208}Pb/^{204}Pb$ = 38.779. The two samples of the mineralization of *La*
288 *Piramide* differ from the one of *Cala Fico*, having $^{206}Pb/^{204}Pb$, $^{207}Pb/^{204}Pb$ and $^{208}Pb/^{204}Pb$ of 18.927
289 - 18.994, 15.666 - 15.668 and 38.928 - 38.961, respectively (Table 1). In Fig. 11, the Pb data of the
290 analyzed veins are displayed along with those of both the sulfide ores from the Iglesiente-Sulcis
291 area (Boni and Koeppel, 1985), and the Cenozoic volcanic rocks of Sardinia (Lustrino et al., 2013).
292 Here, a separation between *Cala Fico* and *La Piramide* deposits can be seen: the sample from *Cala*

293 *Fico* falls in the field of the Sulcis magmatic rocks, whereas the samples from *La Piramide*, having
294 more radiogenic Pb isotope ratios, do not overlap to the Sulcis magmatic rocks and approach the
295 field of some Plio-Pleistocene volcanic rocks outcropping in southern Sardinia (called RPV,
296 radiogenic Pb volcanic rocks, by Lustrino et al., 2000) and marking the passage from the Tertiary
297 orogenic to the Plio-Pleistocene anorogenic volcanism of Sardinia (Lustrino et al., 2007).
298
299

300 **5. Discussion**

301

302 **5.1 Insights into the composition and temperature of the mineralizing fluids**

303 Some insights concerning temperature, composition and pH conditions of the fluids
304 responsible for Mn ore formation can be deduced from the mineralogical assemblage of alteration
305 associated to the mineralization (Browne, 1978; Pirajno, 1992 and references therein).

306 The secondary mineralogical assemblage of host rocks is dominated by phyllosilicates
307 (dioctahedral smectites and, locally, kaolinite) and zeolites. Petrographic evidence indicates that
308 zeolites precede Mn minerals, probably representing post-depositional alteration of the ignimbrite
309 glassy matrix. The mineralogical alteration paragenesis associated to Mn oxides, mainly
310 characterized by smectites with minor kaolinite, identifies an argillic facies and reflects weak acidic
311 conditions (pH indicatively of 5) and relatively low temperature (<150°C) of formation. The low
312 temperature is also confirmed by the occurrence of secondary fluid inclusion assemblages, formed
313 by very small monophase inclusions (< 5 μm), which suggest temperature below 100°C.

314 Inferences on the composition of the mineralizing fluids are obtained by comparing the
315 chemical compositions of the ores and host rock (Fig. 12). The comparison shows that, in addition
316 to Mn, the ores are remarkably enriched in Ba, REE and Y (REY) and Sr and are slightly enriched
317 in Co, Ni, Cu and Zn. This suggests that these elements were introduced by the mineralizing fluids.

318

319 **5.2 Geochemical constraints on the genetic classification of ores and origin of fluids**

320 Several works concerning the genesis of Mn ore deposits have been carried out (Aplin and
321 Cronan, 1985; Halbach et al., 1988; Roy, 1992, 1997; Hein et al., 1997; Hein and Koschinsky,
322 2013; Josso et al., 2017). Mn oxides are deposited in terrestrial and marine environments by
323 hydrogenetic, supergene and hydrothermal processes (Nicholson, 1992, Roy, 1992). In the marine
324 environment these deposits are generally classified into three main categories corresponding to
325 different formation mechanisms (Bonatti et al., 1972; Roy, 1992; Nicholson, 1992; Hein et al.,
326 1997; Bau et al., 2014; Schmidt et al., 2014): hydrogenetic, deriving from precipitation from
327 ambient seawater; diagenetic, deriving from cold porewater below the seafloor during diagenesis;
328 hydrothermal, deriving from precipitation occurred in the vicinity of hydrothermal vents at or below
329 the seafloor. Consequently, the Mn ores forming the mineralization may have different
330 mineralogical components and geochemical compositions. Geochemical features, particularly the
331 contents of transition metals (Mn, Fe, Cu, Co, Ni, Zn, Pb) and As, and contents, ratios and
332 distribution patterns of REY, are the main indicators used to identify different genetic types of Mn
333 mineralization. Accordingly, several classification diagrams were proposed in the literature (Bonatti
334 et al., 1972; Nicholson, 1992; Bau et al., 2014; Josso et al., 2017).

335 In the triangular discrimination diagram (Fig. 13a) recently proposed by Josso et al. (2017),
336 the San Pietro volcanic-hosted Mn ore data (this work and Sinisi et al., 2012), plot very close to the
337 (Fe+Mn)/4 – 100*(Zr+Ce+Y) side of the diagram, describing a trend between the hydrogenetic and
338 hydrothermal end-members. Plotting the data in the discrimination diagrams based on REY,
339 proposed by Bau et al. (2014), these show a trend between the hydrogenetic and hydrothermal fields
340 in the Ce_{SN}/Ce_{SN*} vs Y_{SN}/Ho_{SN} (Fig. 13b), similarly to the previous diagram. In the Ce_{SN}/Ce_{SN*} vs
341 Nd graph (Fig. 13c), on the other hand, part of the San Pietro samples plots in the hydrogenetic
342 field, while some, although showing high Nd in agreement with hydrogenetic features, display

343 negative Ce anomalies. Bau et al. (2014) interpreted this behavior, for marine Mn ores, as due to a
344 mixed hydrothermal-hydrogenetic mechanism, which limited the Ce preferential accumulation by
345 oxidative scavenging from seawater. Combined hydrothermal-hydrogenetic processes have been
346 also proposed for other different types of Mn ore deposits to explain intermediate geochemical
347 features (e.g. Conly et al., 2011, Xiao et al., 2017). Based on the above, we propose that two
348 mechanisms – hydrothermal and hydrogenetic – have been active to give the geochemical
349 characteristics of San Pietro ores. The occurrence of a hydrothermal component, enriched in H_2S,
350 was possibly responsible for the weak acidic (pH around 5) conditions of the mineralizing fluids, as
351 suggested by alteration mineralogy (see 5.1).

352 Regarding the Pb isotopes, the signatures of both *Cala Fico* and *La Piramide* mineralization
353 are clearly distinguishable from those of the sulfide ores from the Iglesiente-Sulcis area, whereas
354 they approach those of the Sardinian Cenozoic volcanic rocks (Fig. 11). However, samples from
355 different veins show a substantial spread in their Pb isotope ratios. Such a spread suggests a
356 contribution of multiple sources of fluids in the genesis of the San Pietro mineralizations. In
357 particular, the *Cala Fico* sample (QM-6v) falls in the field of San Pietro-Sant'Antioco-Sulcis
358 volcanic rocks. Thus, an interaction with hydrothermal fluids circulating in the surrounding
359 volcanic rocks can be inferred in the formation of *Cala Fico* Mn mineralization. The *La Piramide*
360 samples (QM-2v, QM-8v), instead, plot either inside (Fig. 11b) or close (Fig. 11a) to the field of
361 Radiogenic Pb Volcanics (RPV, Lustrino et al., 2000), some of which were emplaced in SW
362 Sardinia not far from San Pietro Island at 11.8 Ma (Isola del Toro). This similarity could indicate
363 the RPV as a plausible additional source of hydrothermal fluids. On the other hand, the Pb isotope
364 ratios of seawater from the Mediterranean Sea at various depths (Fig. 11) define a field that
365 overlaps almost completely the trend delineated by the San Pietro Mn mineralization. Hence, a
366 contribution from seawater can also be envisaged based on the presented data.

The above interpretation differs from the ore-forming model proposed by Sinisi et al. (2012), in which they envisaged the San Pietro volcanic-hosted ores originated from the mixing of magmatic fluids and meteoric waters. Indeed, the relatively low temperature of formation of these Mn mineralizations, estimated by the mineralogical alteration assemblage and the occurrence of monophase secondary fluid inclusions (see 5.1 paragraph), would rule out the involvement of high-temperature magmatic fluids in the genesis of these Mn ores. We must furthermore take into account that, differently from what reported in other Mn ore mineralization on volcanic islands (Liakopoulos et al., 2001; Kilias et al., 2001; Naden et al., 2005; Lykakis and Kilias, 2010; Papavassiliou et al., 2017), no evidence of epithermal mineralization occurs at San Pietro. This indicates that a high temperature hydrothermal (and/or magmatic-hydrothermal) system was not involved in the Mn metallogenesis on the island.

5.3 Mn and REE sources

With the aim of evaluating the absolute mobility of the elements in the host rocks affected by low temperature hydrothermal alteration, and their possible contribution to the mineralization (particularly in terms of Mn and REE contents), we took into account the variation of mass induced by alteration. For this reason, the data were processed using the isocon diagram method (Grant, 1986), which represents a graphical solution of the Gresens (1967) equation (see Appendix).

The isocon diagram (Fig. 14a) shows that Mn substantially behaves as an immobile element and does not undergo any depletion during hydrothermal alteration of San Pietro volcanics. This indicates that volcanic host rocks cannot be viewed as a possible source of Mn for the mineralization on the island. Mn may conversely derive from remobilization of Mn oxides sequestered in shelf and slope sediments and/or by leaching of the older Cenozoic volcanic rocks that form the basement of the island and surroundings. Both sources, as a matter of fact, are in

391 agreement with Pb isotope data (Fig. 11). A possible Mn contribution also from hydrothermal vents
392 into the upwelling seawater masses cannot be excluded.

393 A different behavior is shown by the REE, which result strongly depleted in the
394 hydrothermally altered host rocks (Figs. 14a, b). In this case, volcanic host rock could represent a
395 possible source of the REE found in the mineralization. The similarity between the REE patterns of
396 the Mn mineralization and of the host rocks (Fig. 10) would support this hypothesis. The control
397 exerted by the host rocks over the Mn mineralization, as evidenced by the REE pattern, could be
398 related to the hydrothermal alteration of apatite and monazite, which represent an important storage
399 for REE in magmatic environment, with subsequent leaching of these elements and their re-
400 precipitation within the disseminated hydrothermal cerianite and monazite crystals found in the
401 mineralization (Mongelli et al., 2013).

402 The higher LREE/HREE ratios of the Mn ores (La/Lu = 107-336; Table 1) with respect to
403 the host rocks (La/Lu = 34-88; Table 1) are in agreement with the role played by re-precipitation of
404 hydrothermal LREE-bearing apatite, monazite and cerianite observed in the studied samples (Fig.
405 4F). Furthermore, we must take into account that the REE partitioning between Mn marine ores of
406 hydrogenetic origin and seawater tends to increase the LREE/HREE ratio and Mn oxhydroxide
407 colloidal particles preferentially absorb LREE. Consequently, the influence of a hydrogenetic
408 component (Fig. 13) could have further favored the increase of the LREE/HREE ratio in the Mn
409 mineralization with respect to the host rocks.

410

411 **5.4 Mn metallogenesis**

412 Mineralogical and geochemical data help constraining the conditions of formation of the Mn
413 deposits on San Pietro Island and allow proposing a metallogenetic model. The Ce behavior in the
414 mineralization provides evidence about the oxidation state of the fluid, as Ce is a redox-sensitive
415 REE (Holster, 1997). In oxic environment, soluble Ce^{3+} is oxidized into insoluble Ce^{4+} as CeO_2 and

tends to be rapidly removed from fluid via scavenging by Mn and/or Fe oxyhydroxides or by organic matter in suspension, thus producing a strong negative Ce anomaly in the oxidized waters (Holster, 1997; Pourret et al., 2008). Consequently, Mn mineralizations of hydrogenetic origin are characterized by prominent positive Ce anomalies (Bau et al., 1996, 2014; Pattan et al., 2005; Surya Prakash et al., 2012). The Ce anomaly shown by Mn mineralization of San Pietro Island suggests a shallow, oxidizing environment of deposition. This is in agreement with the absence of Mn carbonates in the ore mineralogy (Fig. 15). The positive Ce anomaly displayed by some samples may also suggest a derivation of Mn from remobilization of hydrogenetic Mn oxides possibly sequestered in shelf and slope sediments (Fig. 16). The reconstruction of eustatic changes of the seawater level in Sardinia area evidenced several episodes of sea level rise during Miocene (Cherchi and Montadert, 1982). As a consequence, we may hypothesize that the sea level rise allowed a later seawater influx within ignimbritic units at San Pietro, after their sub-aerial emplacement, and the development of the shallow water oxidizing conditions that led the deposition of Mn ores.

Assuming an initial pH around 5, caused by the ascent of hydrothermal fluids enriched in H_2S (see 5.1, 5.2 paragraphs), we propose that the precipitation of Mn ore could have been induced by the neutralization of pH of the fluids as a results of water-rock interaction processes (Fig. 15), i.e. hydrolysis reactions. Indeed, in hydrolysis, H^+ is typically consumed by the reaction with silicate minerals, provoking the conversion of anhydrous silicates to hydrous ones (i.e. clay minerals, mainly depending on the temperature) and the release of metal ions into the solution (Pirajno, 1992). This in turn causes the pH increase of the fluid. The occurrence of smectites in the alteration paragenesis associated to our Mn mineralization well agrees with the occurrence of water/rock interaction processes mainly driven by hydrolysis reactions (Fig. 15).

6. Conclusions

441 Geochemical, mineralogical, and isotopic data allowed proposing a metallogenesis model
442 for the San Pietro Island Mn ore deposits.

443 Based on the geochemical relationships characterizing the concentrations of REE and
444 transition metals in different genetic models of Mn oxide deposits, we suggest a mixed
445 hydrothermal-hydrogenetic component in the fluids that formed San Pietro Island Mn deposits (Fig.
446 16). Mn-bearing fluids were originated from the remobilization of Mn oxides sequestered in shelf
447 and slope sediments – providing the hydrogenetic signature – and/or by leaching of the older
448 Cenozoic volcanic rocks. Then these fluids entered the hydrothermal convection, possibly linked to
449 the general thermal anomaly that interested the area from 15 to 12 My (San Pietro, Sant'Antioco,
450 Isola del Toro volcanic activity). The mineralizing fluids, probably dominated by seawater and
451 made acidic by the input of H_2S of hydrothermal origin, were characterized by oxidizing conditions
452 and relatively low temperatures (<100-120°C). The Mn ore deposition occurred in a shallow water
453 environment, as a result of the pH neutralization induced by water-rock interaction processes. The
454 Pb isotopes, although based on a limited number of samples, also agree with the above presented
455 model, as the signatures of the San Pietro veins seem to define a possible multi-component mixing,
456 with contributions from (i) country rocks of San Pietro, (ii) a component similar to the southern
457 Sardinian RPV (e. g. Isola del Toro), and (iii) seawater. Further isotope investigation could help to
458 better define the mode of interaction and the involved components.

459

460

461 Acknowledgements

462 The authors warmly thank M. D'Orazio for help in ICP-MS analysis, G. Ruggieri for help
463 and suggestions on fluid inclusion data and F. Colarieti for assistance during analytical work. We
464 are grateful to S. Agostini for his assistance during the preparation and measurements of the Pb

isotopes. This study was funded by University of Pisa “Fondi d’Ateneo” (MIUR) to AG. We greatly appreciated comments and suggestions by two anonymous reviewers.

Appendix

The isocon method involves plotting elemental abundances of the altered rocks (C^a) against those of the fresh equivalent (C^o) and determining the position of the **isocon** (straight line that joins the points of equal geochemical concentration) by fitting a series of elements assumed to be immobile. The slope of the isocon (M^o/M^a) is the fundamental ratio of equivalent masses before and after alteration (Grant, 1986). In this work, we considered Al, Ti, Zr and Hf as immobile elements. The isocon straight line can be described by the equation:

$$C^a = (M^o/M^a) \cdot C^o \qquad (1)$$

where C^a = concentration of an immobile element in the altered rock, C^o = concentration of an immobile element in the fresh rock, M^a = mass of the altered rock, M^o = mass of the fresh rock. The geometry of the diagram is such that the elements below the isocon are depleted whereas those above are enriched. It is possible to evaluate enrichment or depletion of the various elements by using the following equation:

$$(\Delta C_i/C_i) \cdot 100 = (M^a/M^o) \cdot (C_i^a/C_i^o) - 1 \qquad (2)$$

where $(\Delta C_i/C_i) \cdot 100$ is the percentage variation of the i^{th} element in the altered rock compared with the fresh rock (Grant, 1986).

492 **References**

493

494 Aplin, A.C., Cronan, D.S., 1985. Ferromanganese oxide deposits from the central Pacific
495 Ocean, II. Nodules and associated sediments. Geochim. Cosmochim. Acta 49, 437–451.

496 Bau, M., Koschinsky, A., Dulski, P., Hein, J.R., 1996. Comparison of the partitioning
497 behaviours of yttrium, rare earth elements, and titanium between hydrogenetic marine
498 ferromanganese crusts and seawater. Geochim. Cosmochim. Acta 60, 1709–1725.

499 Bau, M., Schmidt, K., Koschinsky, A., Hein, J.R., Usui, A., 2014. Discriminating between
500 different genetic types of marine ferro-manganese crusts and nodules based on rare earth elements
501 and yttrium. Chem. Geol. 381, 1–9.

502 Bonatti, E., Kraemer, T., Rydell, H., 1972. Classification and genesis of submarine
503 ironmanganese deposits. In: Horn, D. (Ed.), Ferromanganese Deposits on the Ocean Floor. Natl.
504 Sci. Found., Washington, pp. 149–165.

505 Boni, M., Del Vecchio, L., Lirer, L., 1990. Considerazioni sul vulcanismo miocenico della
506 Sardegna sud-occidentale. Atti 75° Congresso Società Geologica Italiana, Milano 1990, Mem. Soc.
507 Geol. Ital. 45, 989-1000.

508 Boni, M., Koeppel, V., 1985. Ore-lead isotope pattern from the Iglesiente-Sulcis area (SW
509 Sardinia) and the problem of remobilization of metals. Mineral. Deposita 20, 185–193.

510 Boni, M., Iannace, A., Balassone, G., 1996. Base metal ores in the Lower Palaeozoic of
511 SouthWestern Sardinia. Econ. Geol. 75th Anniversary Volume, Spec. Publ. 4, pp. 18–28.

512 Botta, P., Salvadori, I., Garbarino, C., Orrù, P.E., Rizzo, R., Cioni, R., Patta, E.D., Puliga,
513 G., Deina, G., Coltorti, M., Gattaceca, J., Mundula, F., 2015. Carta Geologica d'Italia: Isola di San
514 Pietro, Foglio 563, 1:50.000, I.G.M. – ISPRA.
515 http://www.isprambiente.gov.it/Media/carg/563_ISOLA_DI_SAN_PIETRO/Foglio.html

516 Browne, P.R.L., 1978. Hydrothermal alteration in active geothermal fields. Rev. Earth
517 Planet. Sci. 6, 229-250.

518 Catalano, R., Doglioni, C., Merlini, S., 2001. On the Mesozoic Ionian Basin. Geophys. J.
519 Int. 144, 49–64.

520 Cherchi, A., Montadert, L., 1982. Oligo-Miocene rift of Sardinia and the early history of the
521 Western Mediterranean Basin. Nature 298, 736-739.

522 Cioni, R., Salaro, L., Pioli, L., 2001. The Cenozoic volcanism of S. Pietro Island (Sardinia,
523 Italy). Rend. Sem. Facoltà Scienze Università Cagliari, Volume suppl., 71 (2), 149–163.

524 Conly, A.G., Scott, S.D., Bellon, H., 2011. Metalliferous manganese oxide mineralization
525 associated with the Boléo Cu-Co-Zn district, Mexico. Econ. Geol. 106, 1173–1196.

526 Garbarino, C., Lirer, L., Maccioni, L., Salvadori, I., 1990. Isola di San Pietro Carloforte,
527 cenni di geologia e vulcanologia – Edizione della Torre, Cagliari, pp.67. *in Italian*

528 Gisbert, G., Gimeno, D., 2016. Ignimbrite correlation using whole-rock geochemistry: an
529 example from the Sulcis (SW Sardinia, Italy). Geol. Mag. 154, 740–756.

530 Grant, J.A., 1986. The isocon diagram—a simple solution to Gresens' equation for
531 metasomatic alteration. Econ. Geol. 81, 1976–1982.

532 Gresens, R.L., 1967. Composition-volume relationship of metasomatism. Chem. Geol. 2,
533 47–55.

534 Guerin, H., 1983. Origine volcanologènedes gites manganésifères de Sardaigne. Bull. Soc.
535 Geol. Fr. 25, 433–436.

536 Halbach, P., Friedrich, G., Von Stackelberg, U., 1988. The Manganese Nodule Belt of the
537 Pacific Ocean Geological Environment, Nodule Formation, and Mining Aspects. Enke Verlag,
538 Stuttgart, 1988, 245 pp.

539 Hart, S.R., 1984. A large-scale isotope anomaly in the southern hemisphere mantle. Nature
540 309, 753-757.

541 Hein, J.R., Koschinsky, A., 2013. Deep-ocean ferromanganese crusts and nodules. In:
542 Holland, H.D., Turekian, K.K. (Eds.), 2nd Ed. Treatise on Geochemistry vol. 13. Elsevier,
543 Amsterdam, pp. 273–291 (Chapter 11).

544 Hein, J.R., Koschinsky, A., Halbach, P., Manheim, F.T., Bau, M., Kang, J.-K., Lubik, N.,
545 1997. Iron and manganese oxide mineralization in the Pacific. In: Nicholson, K., Hein, J.R., Bühn,
546 B., Dasgupta, S. (Eds.), Manganese Mineralization: Geochemistry and Mineralogy of Terrestrial
547 and Marine Deposits. Geological Society of London Special Publ. 119, 123–138.

548 Holster, W.T., 1997. Evaluation of the application of rare-earth elements to
549 paleoceanography. Palaeogeogr. Palaeoclimatol. Palaeoecol. 132, 309–323.

550 Josso, P., Pelleter, E., Pourret, O., Fouquet, Y., Etoubleau, J., Cheron, S., Bollinger, C.,
551 2017. A new discrimination scheme for oceanic ferromanganese deposits using high field strength
552 and rare earth elements. Ore Geol. Rev. 87, 3–15.

553 Kilias, S.P., Naden, J., Cheliotis, I., Shepherd, T.J., Constandinidou, H., Crossing, J., Simos,
554 I., 2001. Epithermal gold mineralization in the active Aegean volcanic arc: the Profitis Ilias deposit,
555 Milos Island, Greece. Mineral. Deposita 36, 32–44.

556 Lezzerini, M., Tamponi, M., Bertoli, M., 2013. Reproducibility, precision and trueness of X-
557 ray fluorescence data for mineralogical and/or petrographic purposes. Atti Soc. Tosc. Sci. Nat.
558 Mem., Serie A 120, 67–73.

559 Lezzerini, M., Tamponi, M., Bertoli, M., 2014. Calibration of XRF data on silicate rocks
560 using chemicals as in-house standards. Atti Soc. Tosc. Sci. Nat., Mem., Serie A 121, 65–70.

561 Liakopoulos, A., Glasby, G.P., Papavassiliou, C.T., Boulegue, J., 2001. Nature and origin of
562 the Vanimanganese deposit, Milos, Greece: an overview. Ore Geol. Rev. 18, 181–209.

563 Lustrino, M., Fedele, L., Melluso, L., Morra, V., Ronga, F., Geldmacher, J., Duggen, S.,
564 Agostini, S., Cucciniello, C., Franciosi, L., Meisel, T., 2013. Origin and evolution of Cenozoic
565 magmatism of Sardinia (Italy). A combined isotopic (Sr-Nd-Pb-O-Hf-Os) and petrological view.
566 Lithos 180–181, 138–158.

567 Lustrino, M., Melluso, L., Morra, V., 2000. The role of lower continental crust and
568 lithospheric mantle in the genesis of Plio-Pleistocene volcanic rocks from Sardinia (Italy). Earth
569 Planet. Sci. Lett. 180, 259–270.

570 Lustrino, M., Morra, V., Fedele, L., Serracino, M., 2007. The transition between “orogenic”
571 and “anorogenic” magmatism in the western Mediterranean area: the Middle Miocenevolcanic
572 rocks of isola del Toro (SW Sardinia, Italy). Terra Nova 19, 148-159.

573 Lustrino, M., Morra, V., Melluso, L., Brotzu, P., D’Amelio, F., Fedele, L., Franciosi, L.,
574 Lonis, R., Petteruti Liebercknecht, M.A., 2004. The Cenozoic igneous activity of Sardinia. Per.
575 Mineral. 79, 105–134.

576 Lykakis, N., Kilias, S.P., 2010. Epithermal manganese mineralization, Kimolos island,
577 South Aegean volcanic arc, Greece. Bull. Geol. Soc. Greece 43, 2646-2656.

578 McDonough, W.F., Sun, S.S., 1989. Chemical and isotopic systematics of oceanic basalts:
579 implications for mantle composition and processes. Geol. Soc. London Special. Publ. 42, 313–345.

580 McLennan, S.M., 1989. Rare earth elements in sedimentary rocks: influence of provenance
581 and sedimentary processes. Rev. Mineral. Geochem. 21, 169–200.

582 Mongelli, G., Mameli, P., Oggiano, G., Sinisi, R., 2013. Generation of Ce anomalies in SW
583 Sardinian Mn ores. J. Geochem. Expl. 133, 42–49.

584 Moore, M.D., Reynolds, R.C., 1997. X-ray Diffraction and the Identification and Analysis
585 of Clay Minerals. Oxford University Press, Oxford-New–York, 400 pp.

586 Mundula, F., Cioni, R., Rizzo, R., 2009. A simplified scheme for the description of textural
587 features in Welded Ignimbrites: the example of San Pietro Island (Sardinia, Italy). Italian J. Geosci.
588 128, 615–627.

589 Naden, J., Kilias, S.P., Darbyshire, D.P.F., 2005. Active geothermal systems with entrained
590 seawater as modern analogs for transitional volcanic-hosted massive sulfide and continental
591 magmato-hydrothermal mineralization: the example of Milos Island, Greece. Geology 33, 541–544.

592 Nicholson, K., 1992. Contrasting mineralogical-geochemical signatures of manganese
593 oxides: guides to metallogenesis. Econ. Geol. 87, 1253–1264.

594 Palomba, M., Padalino, G., Marchi, M., 2006. Industrial mineral occurrences associated
595 with Cenozoic volcanic rocks of Sardinia (Italy): Geological, mineralogical, geochemical features
596 and genetic implications. Ore Geol. Rev. 29, 118–145.

597 Papavassiliou, K., Voudouris, P., Kanellopoulos, C., Glasby, G., Alfieris, D., Mitsis, I.,
598 2017. New geochemical and mineralogical constraints on the genesis of the Vani hydrothermal
599 manganese deposit at NW Milos island, Greece: Comparison with the Aspro Gialoudi deposit and
600 implications for the formation of the Milos manganese mineralization. Ore Geol. Rev. 80, 594-611.

601 Pattan, J.N., Pearce, N.J.G., Mislankar, P.G., 2005. Constraints in using Cerium anomaly of
602 bulk sediments as an indicator of paleo bottom water redox environment: a case study from the
603 Central Indian Ocean Basin. Chem. Geol. 221, 260–278.

604 Pioli, L., Rosi, M., 2005. Rheomorphic structures in a high-grade ignimbrite: the Nuraxi
605 tuff, Sulcis volcanic district (SW Sardinia, Italy). J. Volcanol. Geotherm. Res. 142, 11–28.

606 Pirajno, F., 1992. Hydrothermal Mineral Deposits. Principles and Fundamental Concepts for
607 the Exploration Geologist. Springer-Verlag, 709 pp.

608 Pourret, O., Davranche, M., Gruau, G., Dia, A., 2008. New insights into cerium anomalies
609 in organic-rich alkaline waters. Chem. Geol. 251, 120–127.

610 Roy, S., 1992. Environments and processes of manganese deposition. Econ. Geol. 87, 1218–
611 1236.

612 Roy, S., 1997. Genetic diversity of manganese deposition in the terrestrial geological record.
613 In: Nicholson, K., Hein, J., Bühn, B., Dasgupta, S. (Eds.), Manganese Mineralisation: Geochemistry
614 and Mineralogy of Terrestrial and Marine Deposits. Geological Society of London Special Publ.
615 119, 5–27.

616 Roy, S., 2006. Sedimentary manganese metallogenesis in response to the evolution of the
617 Earth system. Earth. Sci. Rev. 77, 273–305.

618 Ruggieri, G., Lattanzi, P., Luxoro, S.S., Dessì, R., Benvenuti, M., Tanelli, G., 1997.
619 Geology, mineralogy and fluid inclusion data of the Furtei high-sulfidation gold deposit, Sardinia,
620 Italy. Econ. Geol. 92, 1–19.

621 Schiffman, P., Fridleifsson, G.O., 1991. The smectite-chlorite transition in drillhole NJ-15,
622 Nesjavellir geothermal field, Iceland: XRD, BSE and electron microprobe investigations. J.
623 Metamorph. Geol. 9, 679–696.

624 Schmidt, K., Bau, M., Hein, J., Koschinsky, A., 2014. Fractionation of the geochemical
625 twins Zr-Hf and Nb-Ta during scavenging from seawater by hydrogenetic ferromanganese crusts.
626 Geochim. Cosmochim. Acta. 140, 468–487.

627 Sinisi, R., Mameli, P., Mongelli, G., Oggiano, G., 2012. Different Mn-ores in a continental
628 arc setting: Geochemical and mineralogicasl evidences from Tertiary deposits of Sardinia (Italy).
629 Ore Geol. Rev. 47, 110–125.

630 Speranza, F., Villa, I.M., Sagnotti, L., Florindo, F., Cosentino, D., Cipollari, P., Mattei, M.,
631 2002. Age of the Corsica-Sardinia rotation and Liguro-Provencal basin spreading: new
632 paleomagnetic and Ar/Ar evidence. Tectonophysics 347, 231–251.

633 Stumpf, R., Frank, M., Schonfeld, J., Haley, B., 2010. Late Quaternary variability of
634 Mediterranean outflow water from radiogenic Nd and Pb isotopes. Quat. Sci. Rev. 29, 2462–2472.

635 Surya Prakash, L., Ray, D., Paropkari, A.L., Mudholkar, A.V., Satyanarayanan, M.,
636 Sreenivas, B., Chandrasekharam, D., Kota, D., Kamesh Raju, K.A., Kaisary, S., Balaram, V.,
637 Gurav, T., 2012. Distribution of REEs and yttrium among major geochemical phases of marine Fe–
638 Mn-oxides: comparative study between hydrogenous and hydrothermal deposits. Chem. Geol. 312–
639 313, 127–137.

640 Xiao, J.F., He, J.Y., Yang, H.Y., Wu, C., 2017. Comparison between Datangpo-type
641 manganese ores and modern marine ferromanganese oxyhydroxide precipitates based on rare earth
642 elements. Ore Geol. Rev. 89, 290–308.

643

644

645 **Figure captions**

646 Fig. 1 A. Simplified geological map of San Pietro Island (modified after Botta et al., 2015).
647 The sampling sites (mines of *La Piramide* and *Cala Fico*) are indicated. B. Stratigraphic scheme
648 correlating the volcanic successions of the SPI and the Sulcis mainland with highlight of the
649 sampling sites (modified from Cioni et al., 2001*).*

650 Fig. 2 A. Contact between the Upper Comenditic Ignimbrite (below) and the Monte Ulmus
651 ignimbrite (above) at *La Piramide*. B. Mn ore vein within comenditic ignimbrite. C. Disseminated
652 Mn spots (“ocelli”) in the Upper Comenditic Ignimbrite. D. Argillified volcanics at *La Piramide*. E.
653 Mn veins in the *Cala Fico* comenditic lava flow.

654 Fig. 3 A. Mn-oxide minerals filling cracks and rock porosity in the *La Piramide* ignimbrite
655 host (reflected light, parallel nicols microphoto). B. Fracture-filling texture; note that two Mn
656 minerals can be distinguished by the different reflectivity (reflected light, parallel nicols

657 microphoto). C. Mn-oxide filling void in the ignimbrite, postdating zeolite minerals (reflected light,
658 parallel nicols microphoto). D. Orange clay–rich boundary between the Mn ore vein and the host
659 rock (transmitted light, parallel nicols microphoto).

660 Fig. 4. A. Mn-oxide lining porosity between quartz and feldspar crystals in the ignimbrite
661 (SE image). B. Mn-oxide concretions on quartz crystals (SE image). C, D. Mn-oxide mineralization
662 filling open spaces in the host-rock matrix. Dark areas are formed by K-rich Mn oxide; light areas
663 are formed by Ba-rich Mn oxide (BSE images). E. K-feldspar phenocryst surrounded by Mn
664 mineralization. Brightest areas are due to the occurrence of micron-sized Ce oxides closely
665 associated to Mn oxides (BSE image). F. Particular of Mn oxide mineralization with associated Ce-
666 oxide enrichment (BSE image). G. Clay minerals (smectites) on the hydrothermally altered
667 comenditic host rock (BSE image). H. Zeolites as alteration of the ignimbrite unit at La Piramide
668 (BSE image).

669 Fig. 5 A, B. Microphotographs of secondary trails of monophase (liquid) fluid inclusions
670 within quartz crystals in the *La Piramide* Mn ores. C. Enlargement of A, which takes in evidence
671 the secondary trails of fluid inclusion.

672 Fig. 6 Representative X-ray diffraction patterns of (a) San Pietro mineralization Mn oxides
673 with peak positions provided for cryptomelane (Cry), hollandite (Hol) and possibly pyrolusite (Pyr).
674 Quartz (Qz) and sanidine (Sa) peak positions are also indicated; (b) 001 reflection of smectite from
675 the gangue of the Mn mineralization, on oriented mounts (blue: Mg^{2+} saturated in air dried state,
676 green: Mg^{2+} saturated and ethylene glycol solvated, orange: K^{+} saturated and heated at 60°C,
677 yellow: K^{+} saturated and heated at 300°C, red: K^{+} saturated and heated at 550°C); (c) kaolinite
678 (Kln) from *La Piramide* Mn mineralization. Quartz (Qz) and albite (Ab) peak positions are also
679 indicated.

680 Fig. 7 Analyses of smectites associated with Mn ores plotted on the sum of the major non-
681 interlayer cations (Si + Al + Fe + Mg) vs. Al diagram proposed by Schiffman and Fridleifsson
682 (1991). All analyses recalculated on 28 oxygens basis.

683 Fig. 8 Selected major and trace elements variation diagrams vs MnO (wt%) for Mn ore
684 mineralization and host rock. Sinisi et al. (2012) data are reported for comparison (VH2 and VH3
685 samples from La Piramide and Cala Fico, respectively).

686 Fig. 9 Total alkali vs. SiO_2 (TAS) diagram of host rock samples of San Pietro Mn
687 mineralization. Gray field represents the San Pietro volcanic rocks (from Lustrino et al., 2013 and
688 Gisbert and Gimeno, 2016)

689 Fig. 10 Chondrite-normalized REE patterns of San Pietro Island Mn-ore (black) and host
690 rock (red) samples. Chondrite normalizing values from Mc Donough and Sun (1989). REE data on
691 San Pietro Mn ore from Sinisi et al. (2012) are reported for comparison (gray area).

692 Fig. 11 (a) $^{207}Pb/^{204}Pb$ and (b) $^{208}Pb/^{204}Pb$ vs. $^{206}Pb/^{204}Pb$ for San Pietro Mn mineralization
693 compared with the Pb isotope data of San Pietro, Sant'Antioco, Sulcis and Isola del Toro and RPV
694 (Radiogenic Pb Volcanics, see Lustrino et al. 2000) volcanic rocks (Lustrino et al., 2013) and ore
695 sulfides from the Sulcis Iglesiente area (Boni and Koeppel, 1985). Mediterranean seawater field
696 (Stumpf et al. 2010) is also reported for comparison. NHRL: Northern Hemisphere Reference Line
697 (Hart, 1984).

698 Fig. 12 Histogram showing the comparison of trace element concentration between host
699 rock and Mn ore.

700 Fig. 13 (a) Plot of San Pietro Island Mn ore composition on ternary discriminative graph for
701 genetic classification of Fe-Mn deposits after Josso et al. (2017). (b) Ce_{SN}/Ce_{SN}^* vs. Y_{SN}/Ho_{SN} and
702 (c) Ce_{SN}/Ce_{SN}^* vs. Nd concentration diagrams of San Pietro Island Mn ores, based on Bau et al.
703 (2014). Subscript "SN"; shale is Post-Archean Australian Shale, PAAS, of McLennan (1989). Sinisi

et al. (2012) data are reported for comparison (VH2 and VH3 samples from La Piramide and Cala Fico, respectively).

Fig. 14 (a), (b) Isocon diagram (upper) and histogram showing percentage of gains and losses (bottom) of selected elements during hydrothermal alteration of Mn mineralization host rock, as calculated from isocon diagram method (see Appendix). Variation of +4 to +1 = a gain of more than 100%, 50 to 100%, 25 to 50% and 10 to 25%, respectively. 0 = immobile elements (variation in the range +10 and -10%). Values of -1 to -4 = losses of 10 to 25%, 25 to 50%, 50 to 90%, more than 90%, respectively.

Fig. 15 Eh-pH diagram showing the stability of Mn oxide and Mn carbonates deposits in natural water (after Roy, 2006, modified). The diagram is built assuming Mn^{2+}; total carbonates and sulfur concentrations of 10^{-6}, 1 and 10^{-6} M respectively, according to Roy (2006). The dashed lines enclose the boundary of natural water. The dark gray circle represents the indicative Eh-pH conditions of the ore forming fluid at San Pietro Island; the dashed arrow indicates the shift of the Eh-pH conditions that led to Mn ore precipitation (see text for details).

Fig. 16 Schematic sketch of the metallogenic model of San Pietro Island Mn mineralization. The insert represents the scheme of a typical Mn-oxide vein within the ignimbrite host rock, bounded by clay-rich rims produced as a consequence of water/rock interaction processes (see text for explanation).

Table captions

Table 1 Geochemical analysis of Mn ores and of host rocks. For ignimbrite, both the bulk ignimbrite close to the veins and the unaltered juveniles out of the mineralized area have been analyzed. Fe_2O_{3T}: all Fe expressed as Fe_2O_3 wt%; L.O.I.: Loss on Ignition; bdl: below detection limit; -: not analyzed; Ce and Eu anomalies calculated with chondrite-normalized values

728 (normalization values from McDonough and Sun, 1989). Pb isotope ratios: errors quoted are within
729 run; the external reproducibility is between ± 0.016 and ±0.018% (2 S.D.) for all ratios.

730 Table 2 EDS analysis of Mn ores and alteration mineral in representative samples of La
731 Piramide and Cala Fico sites. Smectite formulas calculated based on 22 oxygens. Cry =
732 Cryptomelane; Hol = Hollandite; Mnz = Monazite; Sm = Smectite; - : not analyzed.

733

734

A

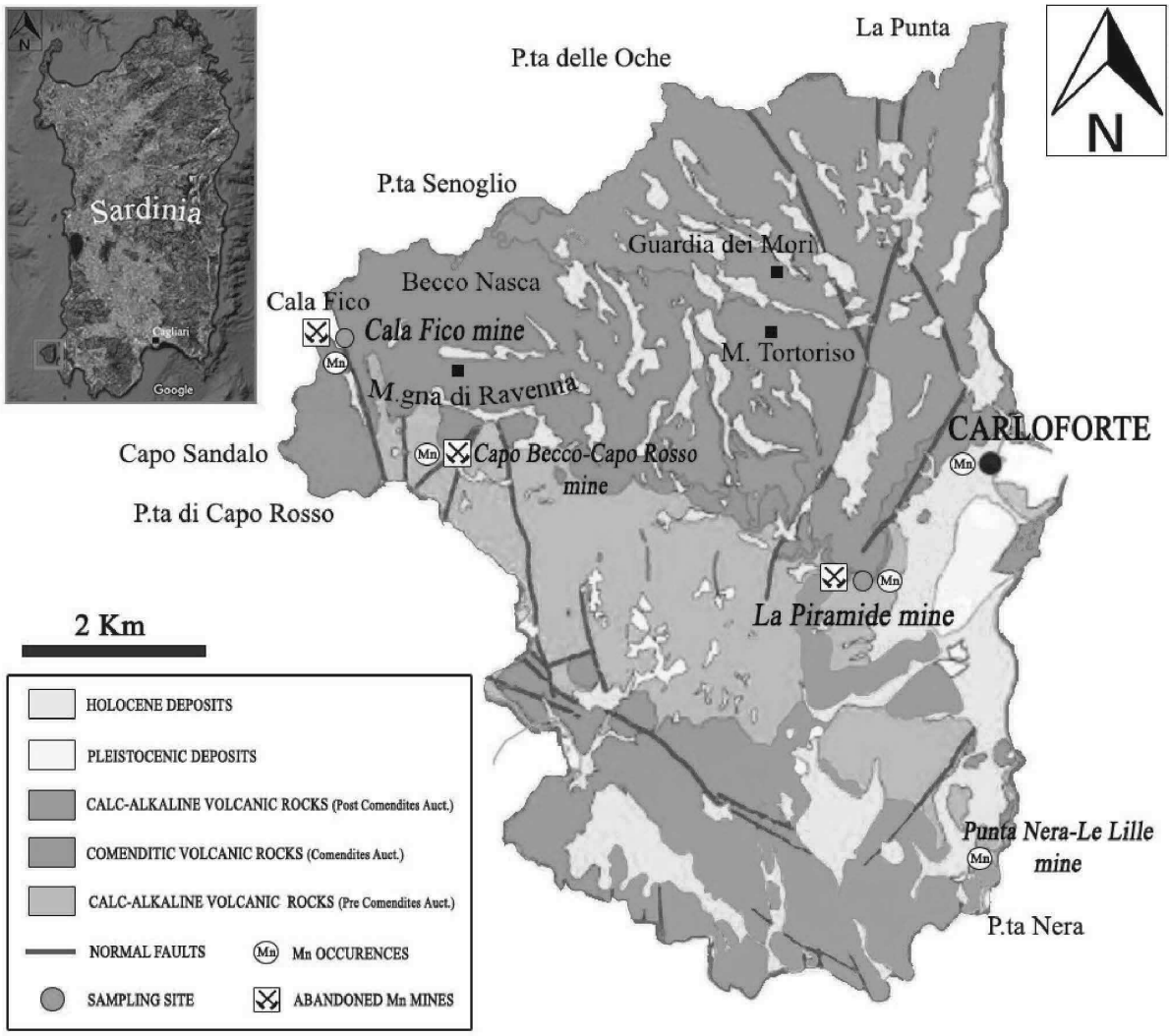
Sardinia
Cagliari
Google
N
La Punta
P.ta delle Oche
P.ta Senoglio
Guardia dei Mori
Becco Nasca
Cala Fico
Cala Fico mine
M. Tortoriso
M.gna di Ravenna
CARLOFORTE
Capo Sandalo
Capo Becco-Capo Rosso mine
P.ta di Capo Rosso
La Piramide mine
Punta Nera-Le Lille mine
P.ta Nera
2 Km
HOLOCENE DEPOSITS
PLEISTOCENIC DEPOSITS
CALC-ALKALINE VOLCANIC ROCKS (Post Comendites Auct.)
COMENDITIC VOLCANIC ROCKS (Comendites Auct.)
CALC-ALKALINE VOLCANIC ROCKS (Pre Comendites Auct.)
NORMAL FAULTS
Mn OCCURENCES
SAMPLING SITE
ABANDONED Mn MINES

B

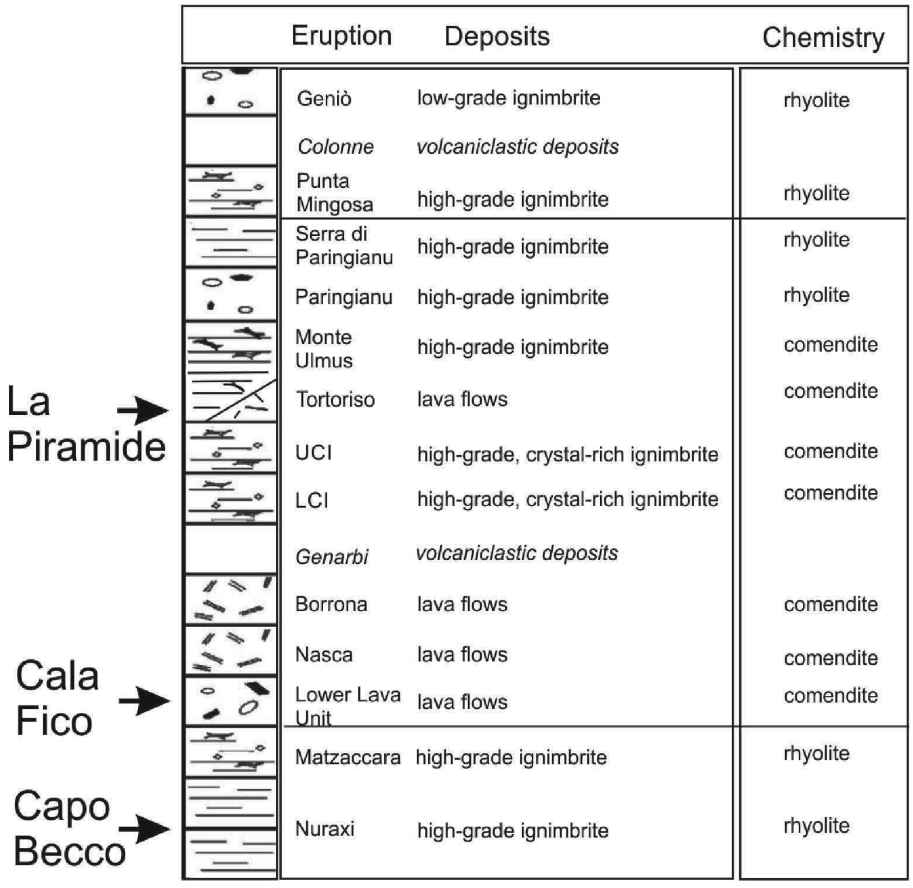
Eruption
Deposits
Chemistry
Geniò
low-grade ignimbrite
rhyolite
Colonne
volcaniclastic deposits
Punta Mingosa
high-grade ignimbrite
rhyolite
Serra di Paringianu
high-grade ignimbrite
rhyolite
Paringianu
high-grade ignimbrite
rhyolite
Monte Ulmus
high-grade ignimbrite
comendite
Tortoriso
lava flows
comendite
La Piramide
UCI
high-grade, crystal-rich ignimbrite
comendite
LCI
high-grade, crystal-rich ignimbrite
comendite
Genarbi
volcaniclastic deposits
Borrona
lava flows
comendite
Nasca
lava flows
comendite
Cala Fico
Lower Lava Unit
lava flows
comendite
Matzaccara
high-grade ignimbrite
rhyolite
Capo Becco
Nuraxi
high-grade ignimbrite
rhyolite

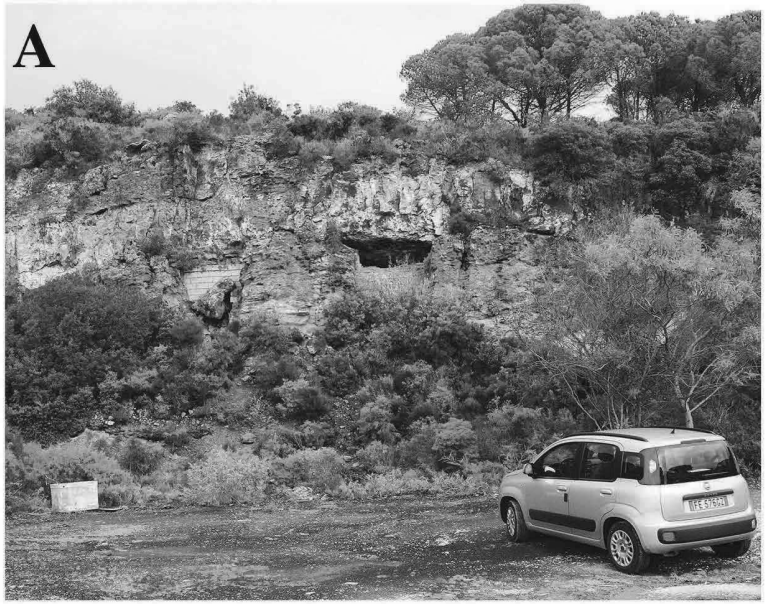
A


C


B

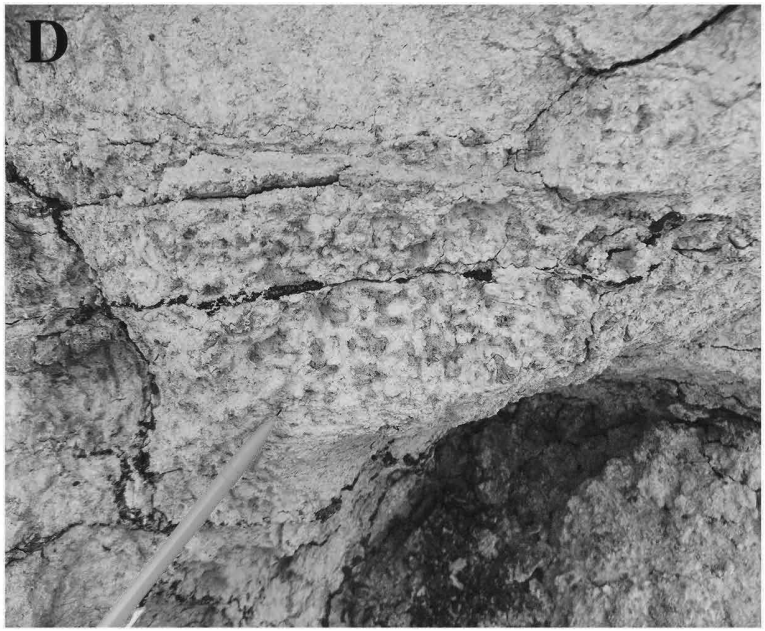
D

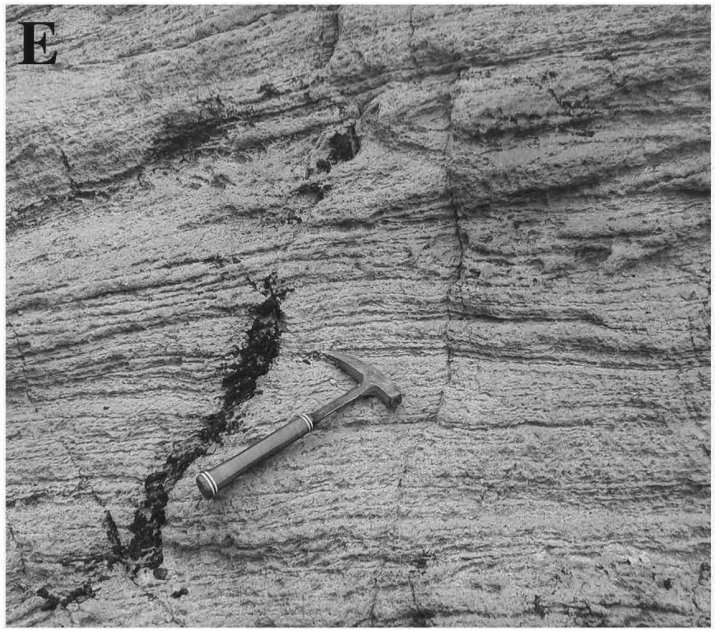
E

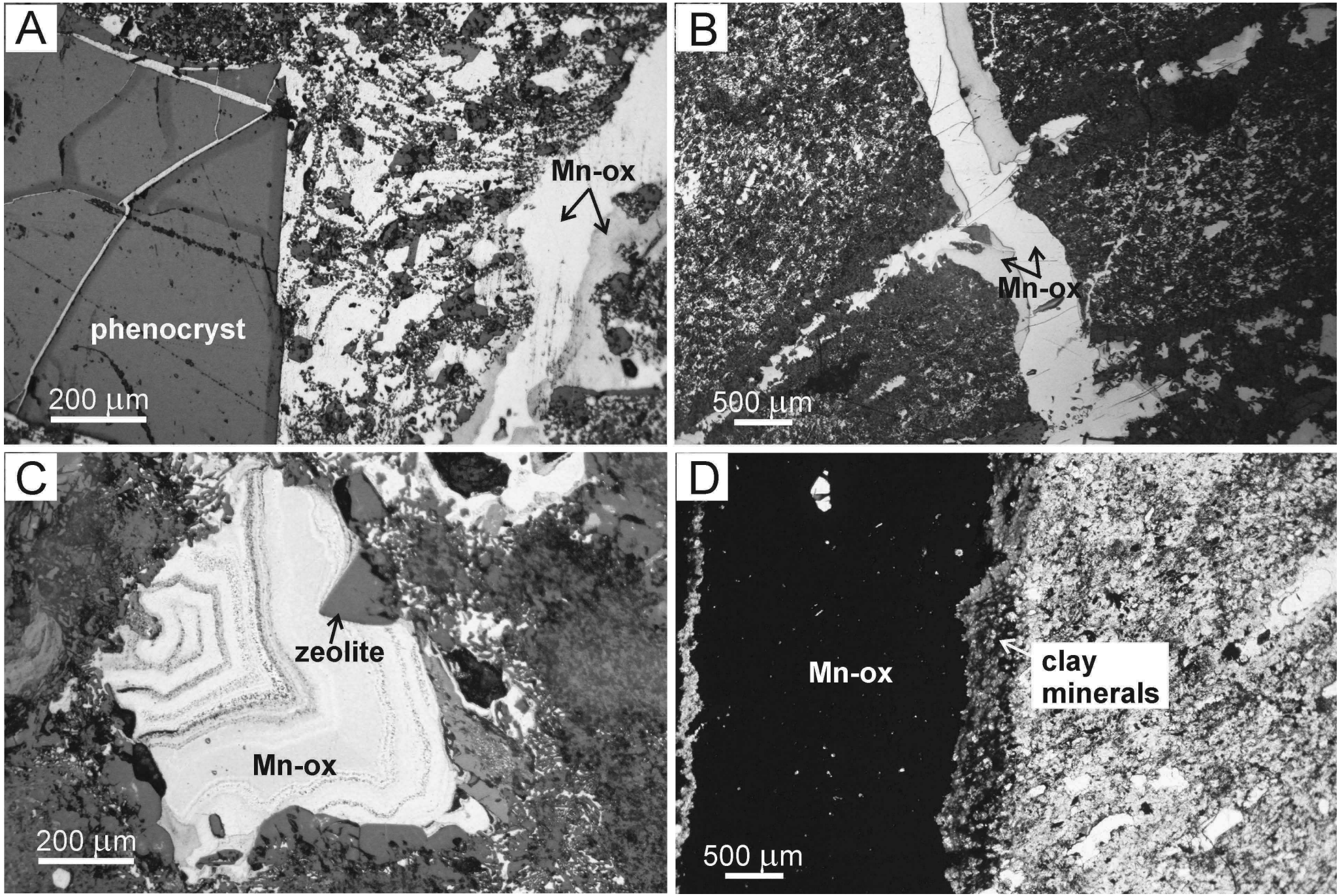
A
Mn-ox
phenocryst
200 μm
B
Mn-ox
500 μm
C
zeolite
Mn-ox
200 μm
D
Mn-ox
clay
minerals
500 μm

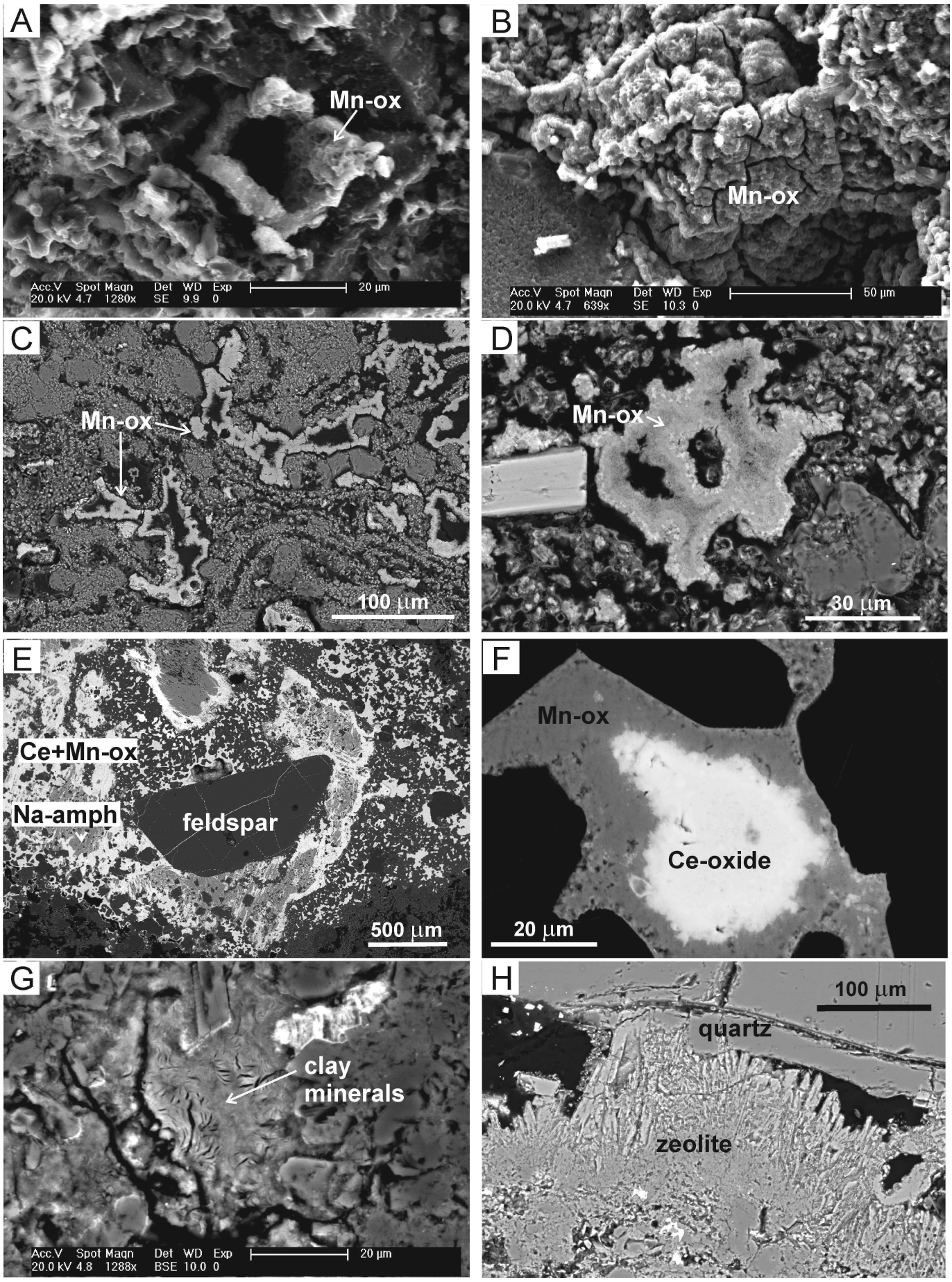
A
Mn-ox
Acc.V Spot Magn Det WD Exp
20.0 kV 4.7 1280x SE 9.9 0
20 µm
B
Mn-ox
Acc.V Spot Magn Det WD Exp
20.0 kV 4.7 639x SE 10.3 0
50 µm
C
Mn-ox
100 µm
D
Mn-ox
30 µm
E
Ce+Mn-ox
Na-amph
feldspar
500 µm
F
Mn-ox
Ce-oxide
20 µm
G
clay
minerals
Acc.V Spot Magn Det WD Exp
20.0 kV 4.8 1288x BSE 10.0 0
20 µm
H
100 µm
quartz
zeolite

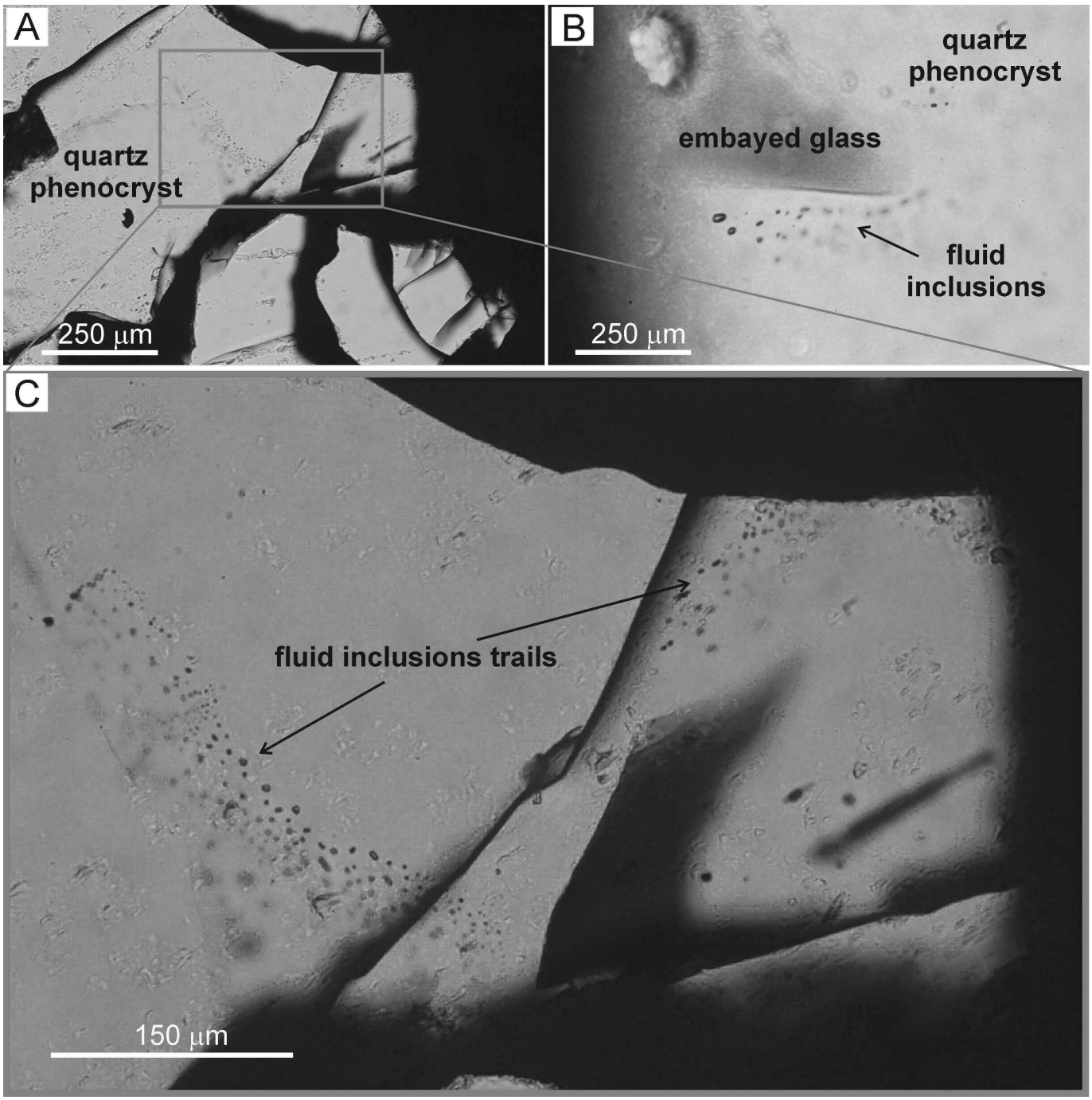
A
quartz
phenocryst
250 μm
B
quartz
phenocryst
embayed glass
fluid
inclusions
250 μm
C
fluid inclusions trails
150 μm

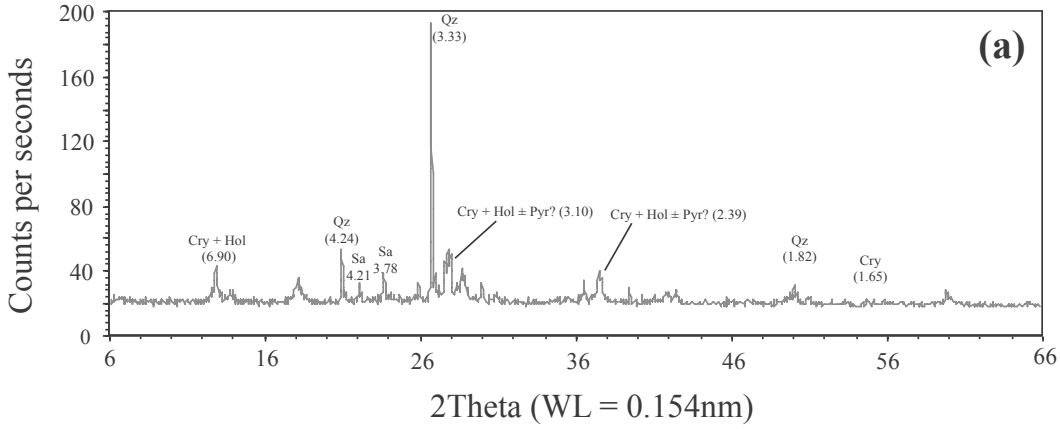
(a)
Counts per seconds
2Theta (WL = 0.154nm)
Qz (3.33)
Cry + Hol (6.90)
Qz (4.24)
Sa 4.21
Sa 3.78
Cry + Hol ± Pyr? (3.10)
Cry + Hol ± Pyr? (2.39)
Qz (1.82)
Cry (1.65)

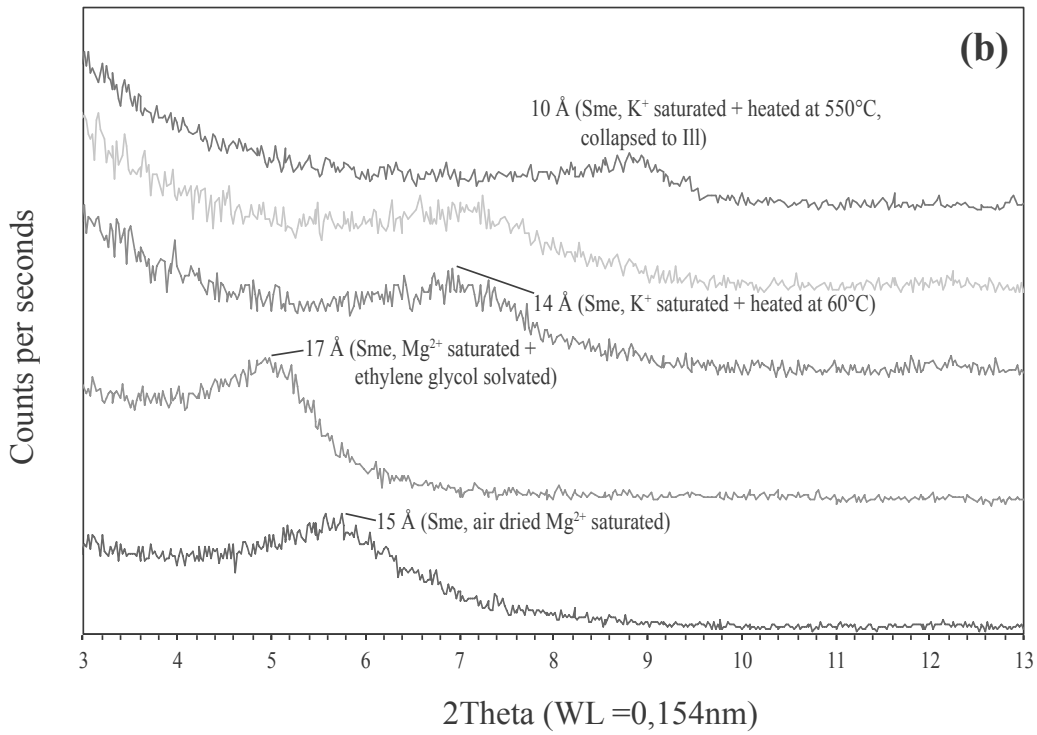
(b)
Counts per seconds
2Theta (WL =0,154nm)
10 Å (Sme, K+ saturated + heated at 550°C, collapsed to Ill)
14 Å (Sme, K+ saturated + heated at 60°C)
17 Å (Sme, Mg2+ saturated + ethylene glycol solvated)
15 Å (Sme, air dried Mg2+ saturated)

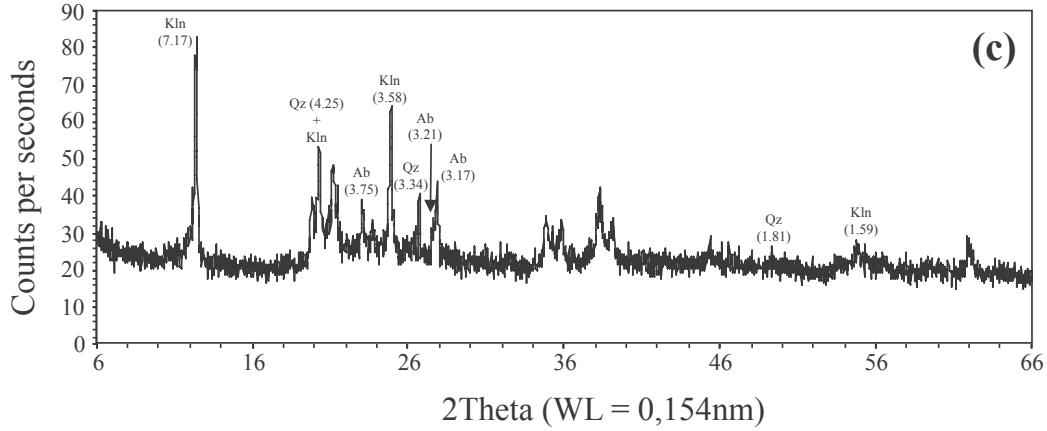
(c)
Counts per seconds
2Theta (WL = 0,154nm)
Kln (7.17)
Qz (4.25) + Kln
Kln (3.58)
Ab (3.21)
Ab (3.75)
Qz (3.34)
Ab (3.17)
Qz (1.81)
Kln (1.59)

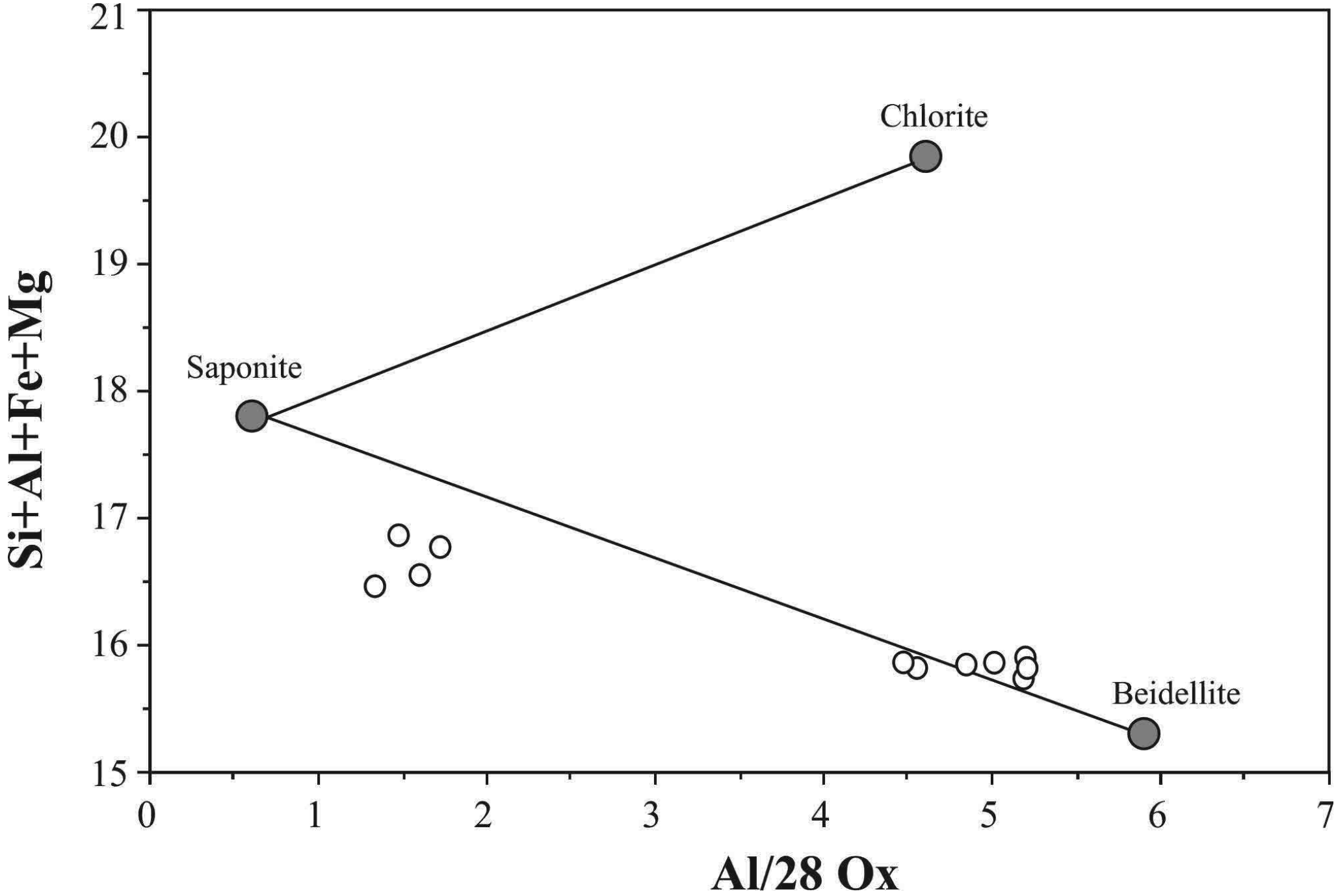
Chlorite
Saponite
Beidellite
Si+Al+Fe+Mg
Al/28 Ox
21
20
19
18
17
16
15
0
1
2
3
4
5
6
7

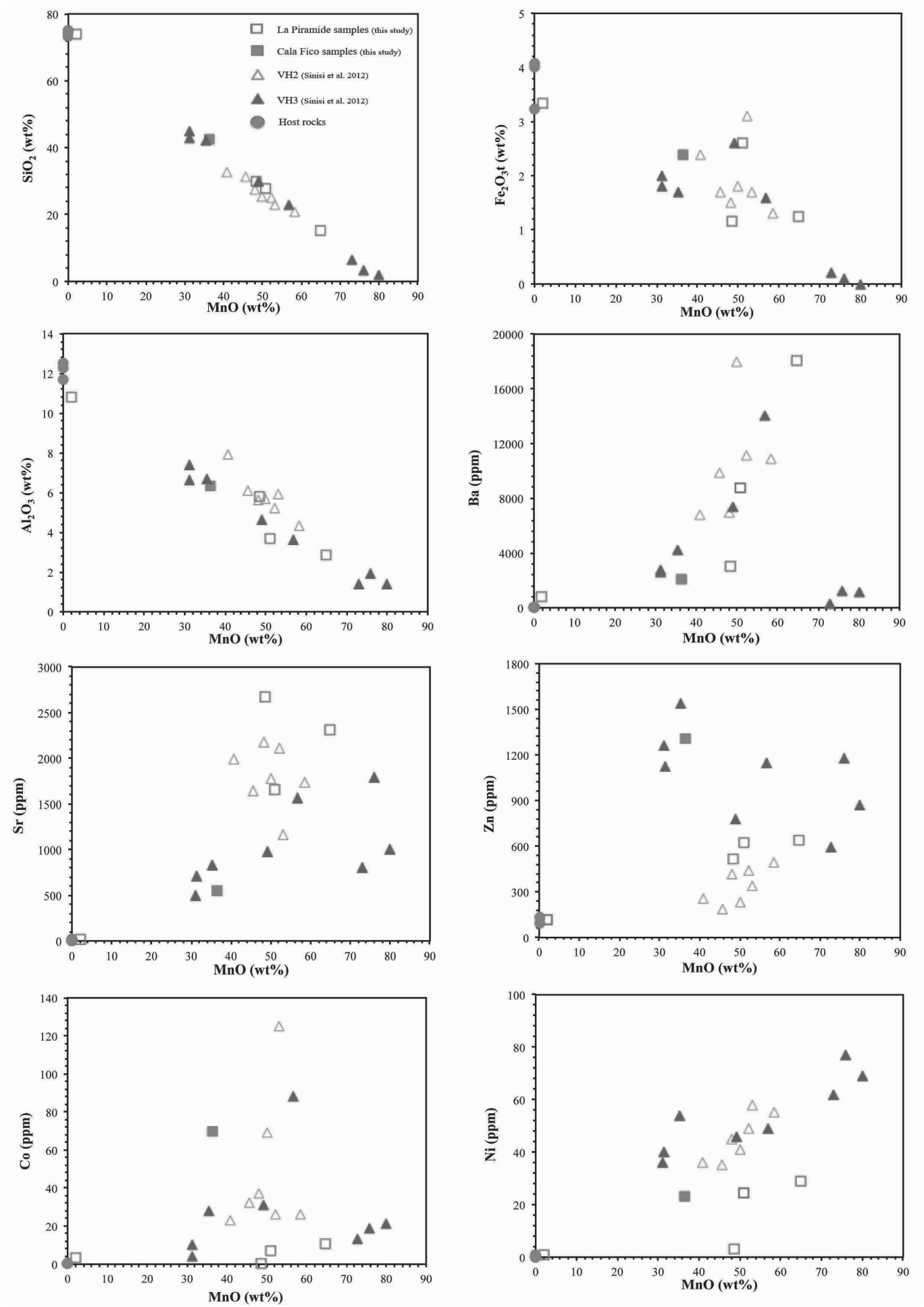
La Piramide samples (this study)
Cala Fico samples (this study)
VH2 (Sinisi et al. 2012)
VH3 (Sinisi et al. 2012)
Host rocks
SiO2 (wt%)
Fe2O3t (wt%)
Al2O3 (wt%)
Ba (ppm)
Sr (ppm)
Zn (ppm)
Co (ppm)
Ni (ppm)
MnO (wt%)

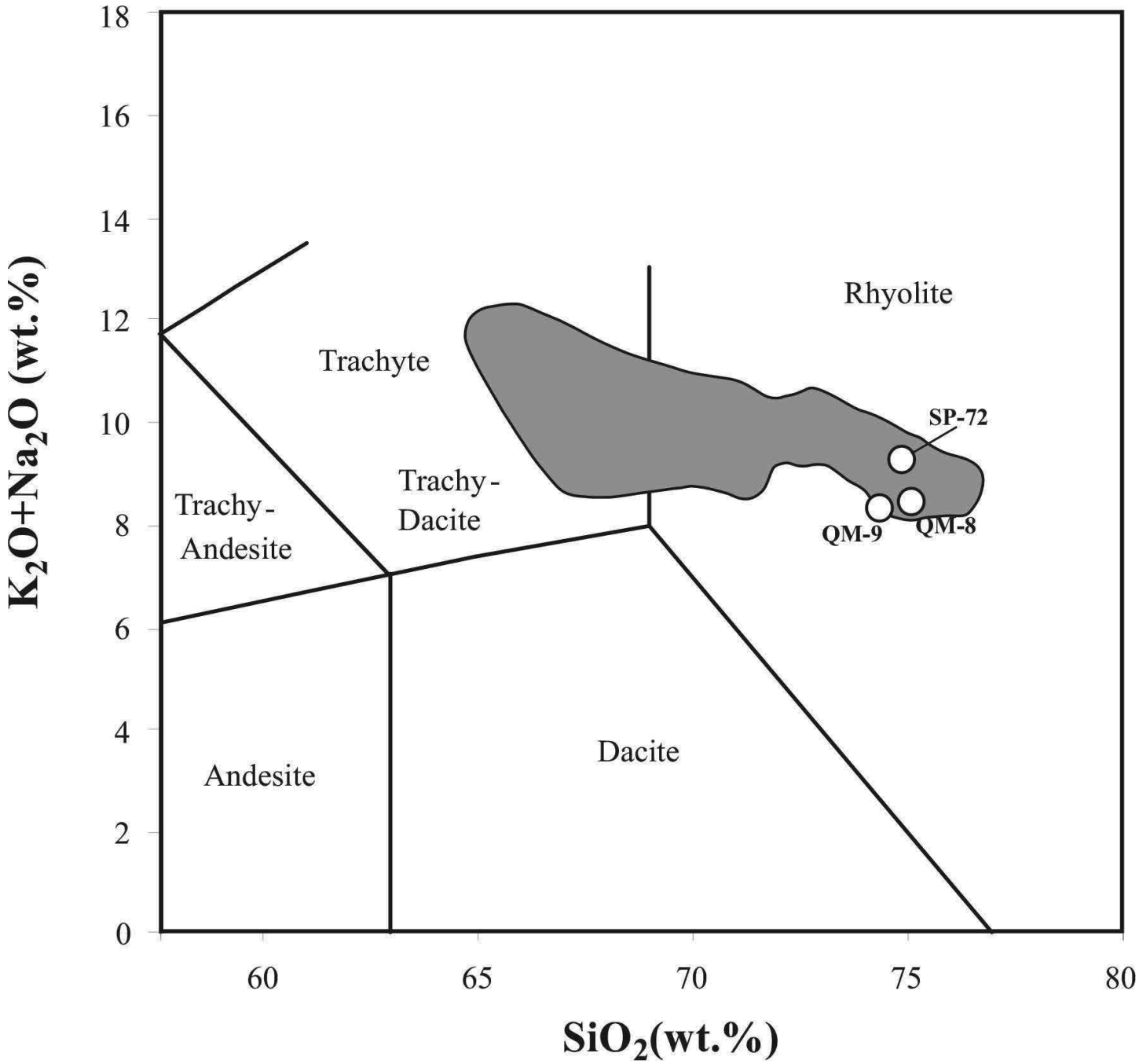
18
16
14
12
10
8
6
4
2
0
60
65
70
75
80
K_2O+Na_2O (wt.%)
SiO_2(wt.%)
Rhyolite
Trachyte
Trachy-
Andesite
Trachy-
Dacite
Andesite
Dacite
SP-72
QM-9
QM-8

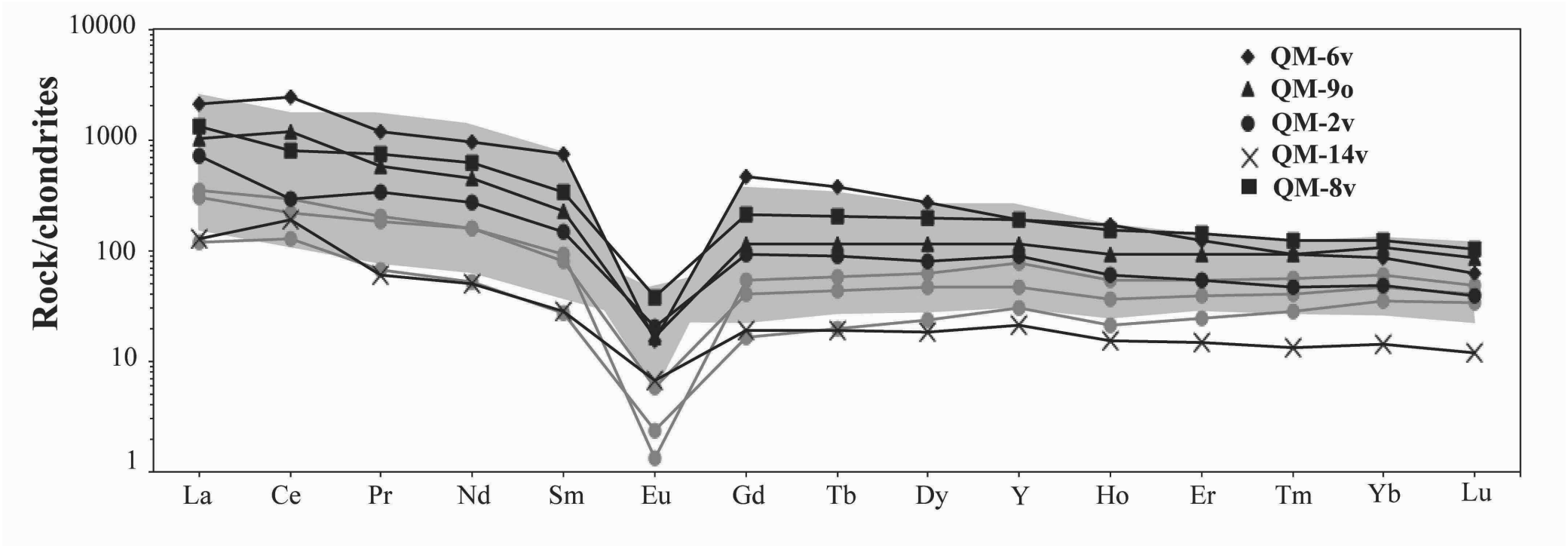
Rock/chondrites
10000
1000
100
10
1
La
Ce
Pr
Nd
Sm
Eu
Gd
Tb
Dy
Y
Ho
Er
Tm
Yb
Lu
QM-6v
QM-9o
QM-2v
QM-14v
QM-8v

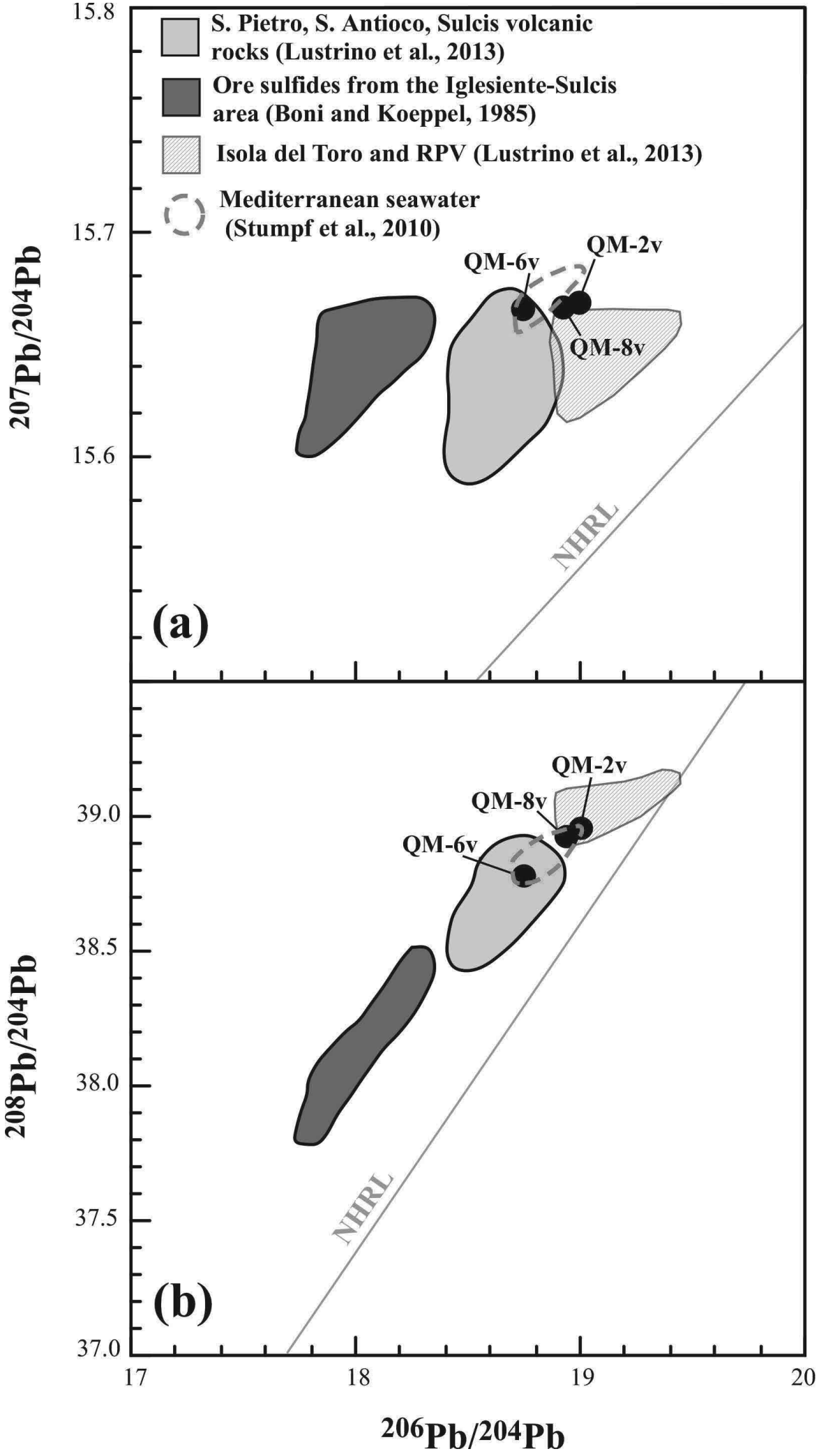
S. Pietro, S. Antioco, Sulcis volcanic rocks (Lustrino et al., 2013)
Ore sulfides from the Iglesiente-Sulcis area (Boni and Koeppel, 1985)
Isola del Toro and RPV (Lustrino et al., 2013)
Mediterranean seawater (Stumpf et al., 2010)
QM-6v
QM-2v
QM-8v
NHRL
(a)
(b)
15.8
15.7
15.6
39.0
38.5
38.0
37.5
37.0
17
18
19
20
$^{207}Pb/^{204}Pb$
$^{208}Pb/^{204}Pb$
$^{206}Pb/^{204}Pb$

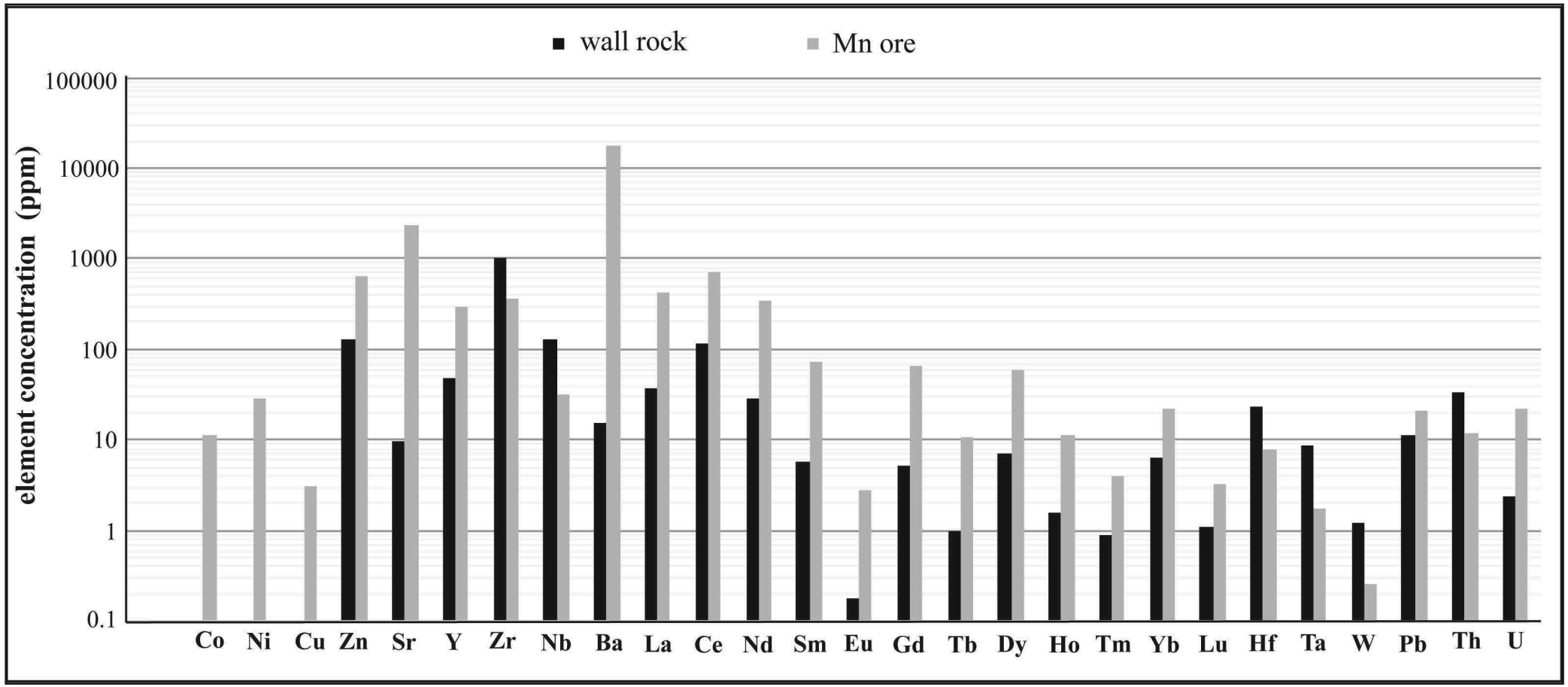
wall rock
Mn ore
element concentration (ppm)
100000
10000
1000
100
10
1
0.1
Co
Ni
Cu
Zn
Sr
Y
Zr
Nb
Ba
La
Ce
Nd
Sm
Eu
Gd
Tb
Dy
Ho
Tm
Yb
Lu
Hf
Ta
W
Pb
Th
U

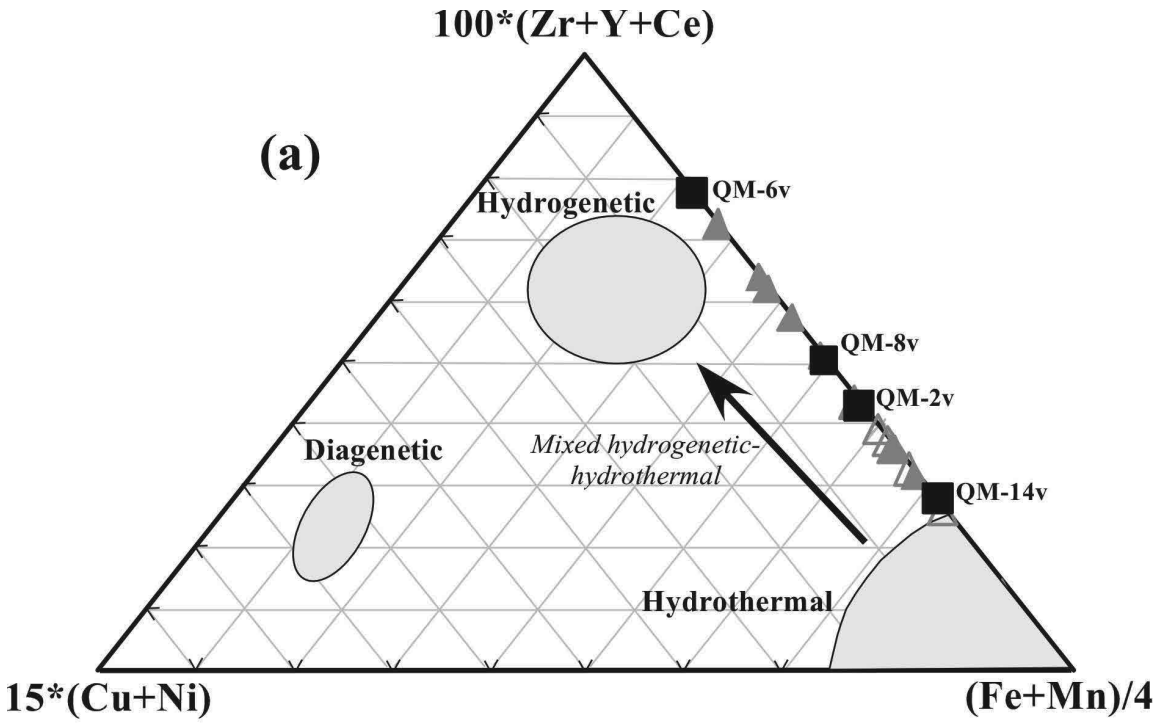
100*(Zr+Y+Ce)
(a)
Hydrogenetic
QM-6v
QM-8v
QM-2v
QM-14v
Diagenetic
Mixed hydrogenetic-hydrothermal
Hydrothermal
15*(Cu+Ni)
(Fe+Mn)/4

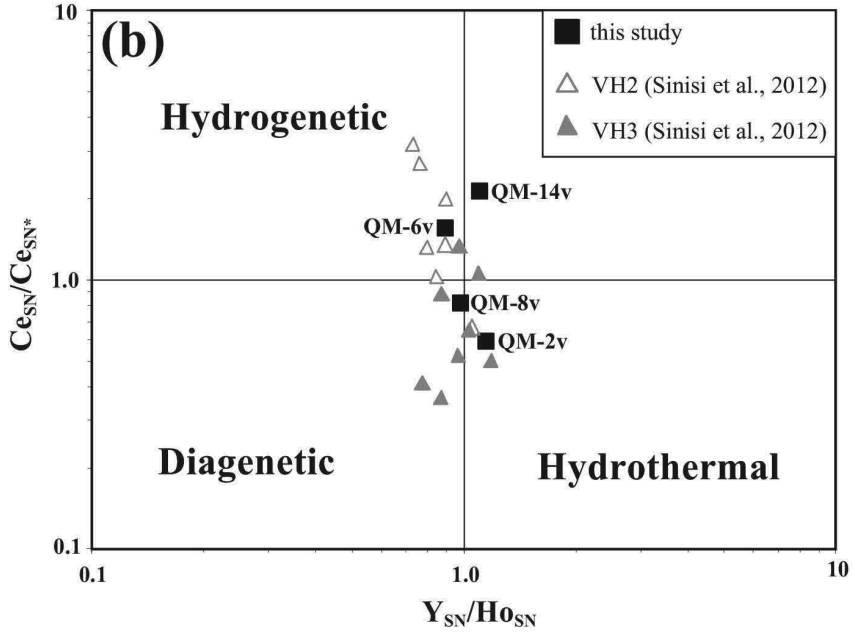
(b)
this study
VH2 (Sinisi et al., 2012)
VH3 (Sinisi et al., 2012)
Hydrogenetic
QM-14v
QM-6v
QM-8v
QM-2v
Diagenetic
Hydrothermal
10
1.0
0.1
0.1
1.0
10
Ce_SN/Ce_SN*
Y_SN/Ho_SN

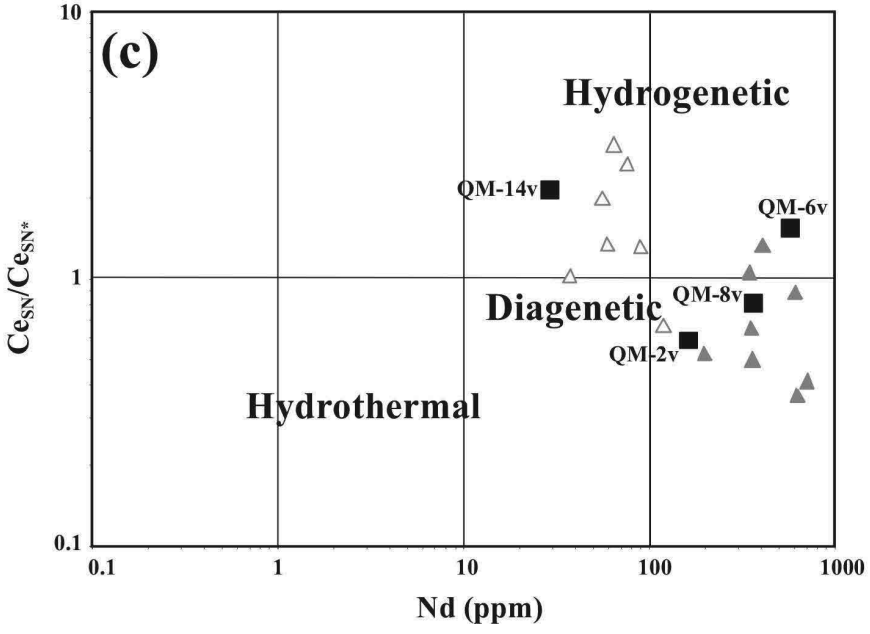
(c)
Hydrogenetic
QM-14v
QM-6v
QM-8v
Diagenetic
QM-2v
Hydrothermal
10
1
0.1
0.1
1
10
100
1000
Ce_SN/Ce_SN*
Nd (ppm)

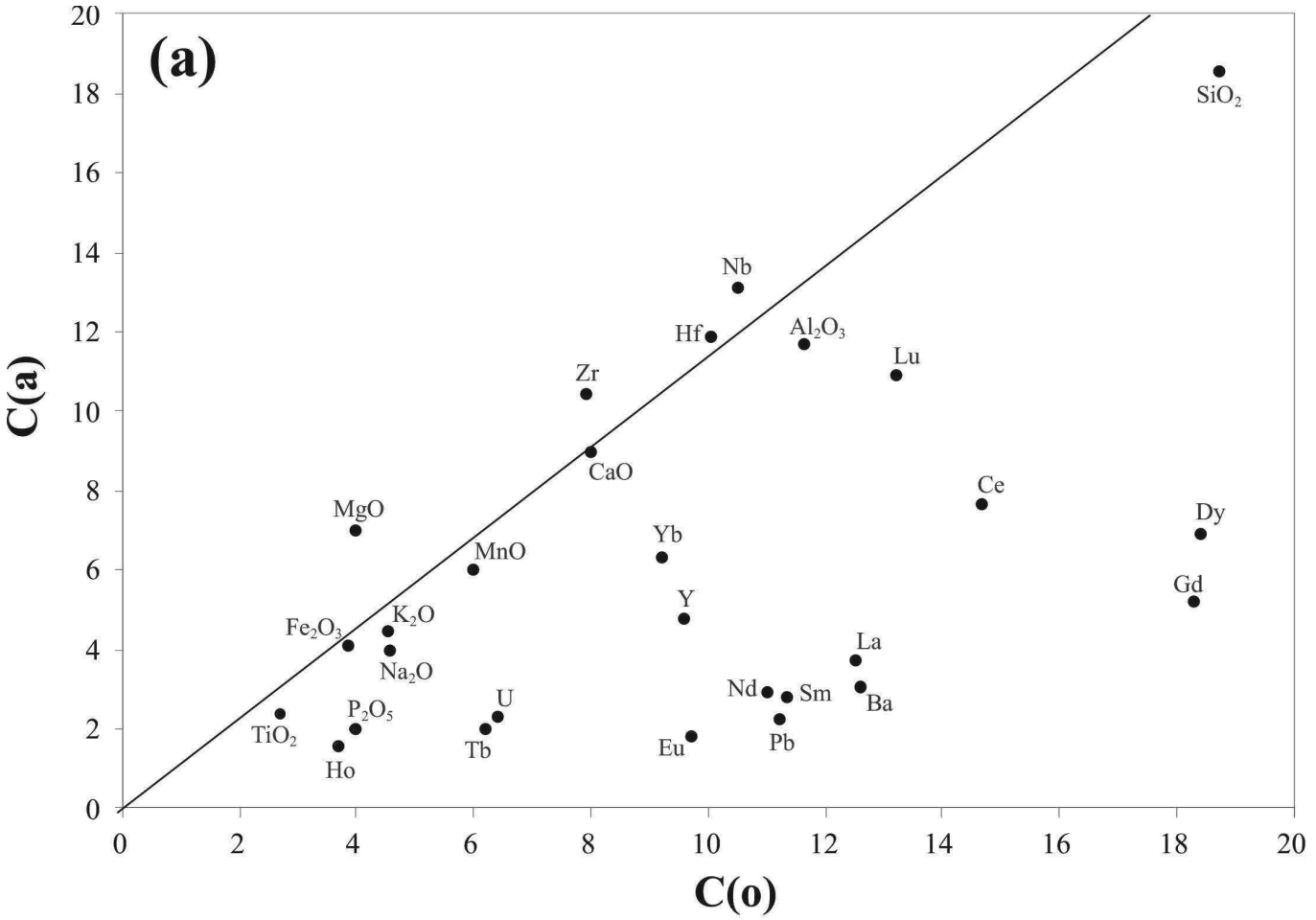
(a)
C(a)
C(o)
0
2
4
6
8
10
12
14
16
18
20
SiO2
Nb
Hf
Al2O3
Lu
Zr
CaO
Ce
Dy
MgO
Yb
MnO
Gd
Y
Fe2O3
K2O
La
Na2O
Nd
Sm
Ba
U
P2O5
TiO2
Pb
Tb
Eu
Ho

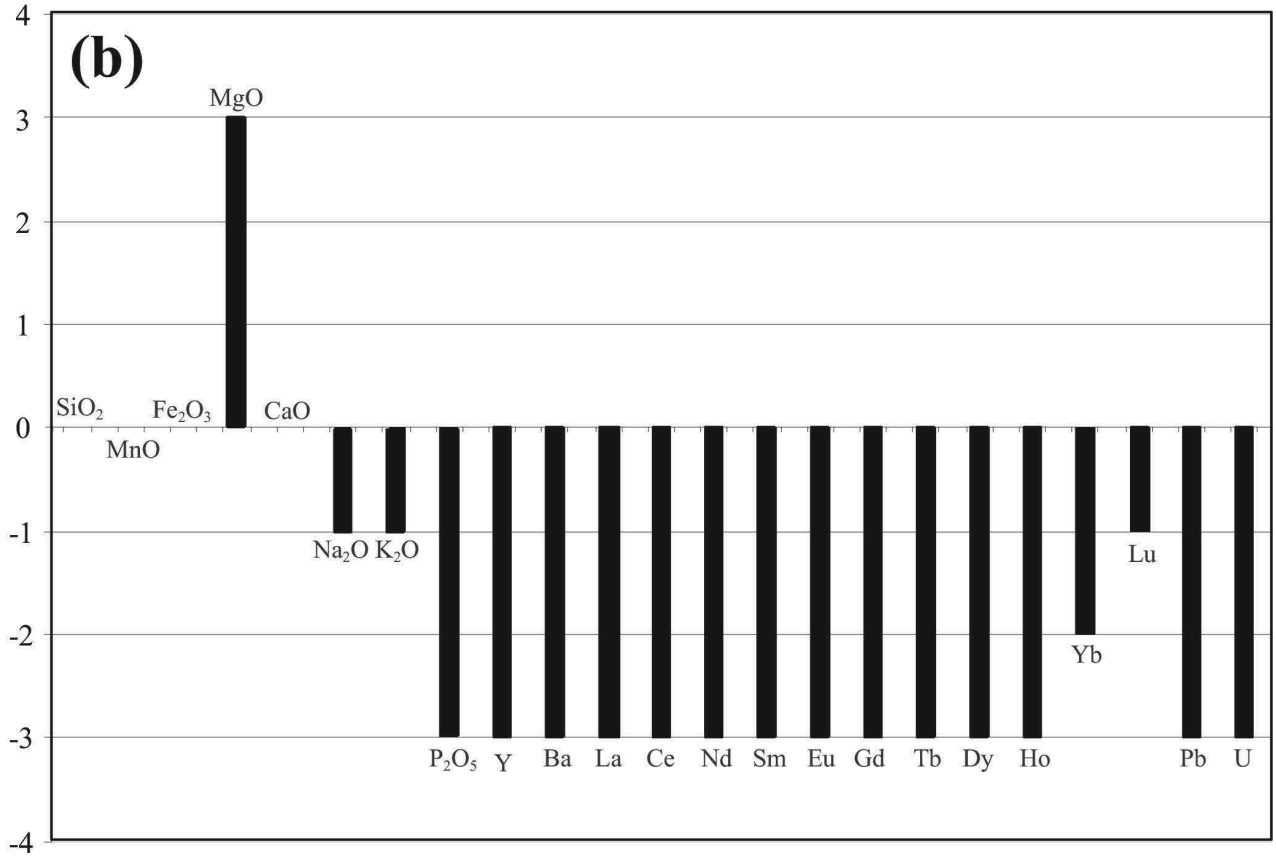
(b)
4
3
2
1
0
-1
-2
-3
-4
MgO
SiO2
Fe2O3
CaO
MnO
Na2O
K2O
Lu
Yb
P2O5
Y
Ba
La
Ce
Nd
Sm
Eu
Gd
Tb
Dy
Ho
Pb
U

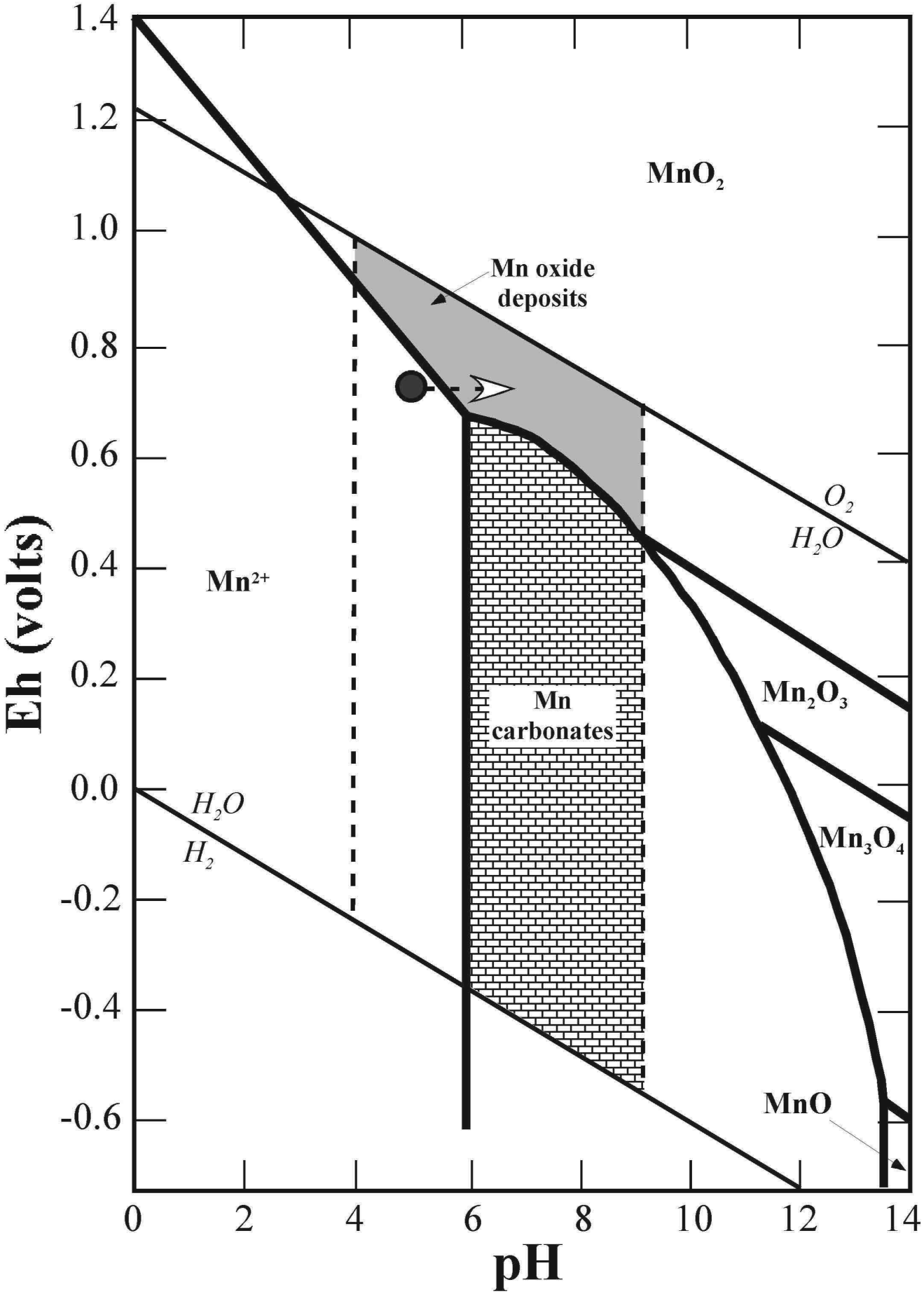
1.4
1.2
1.0
0.8
0.6
0.4
0.2
0.0
-0.2
-0.4
-0.6
Eh (volts)
0
2
4
6
8
10
12
14
pH
MnO2
Mn oxide deposits
Mn2+
O2
H2O
Mn2O3
Mn carbonates
H2O
H2
Mn3O4
MnO

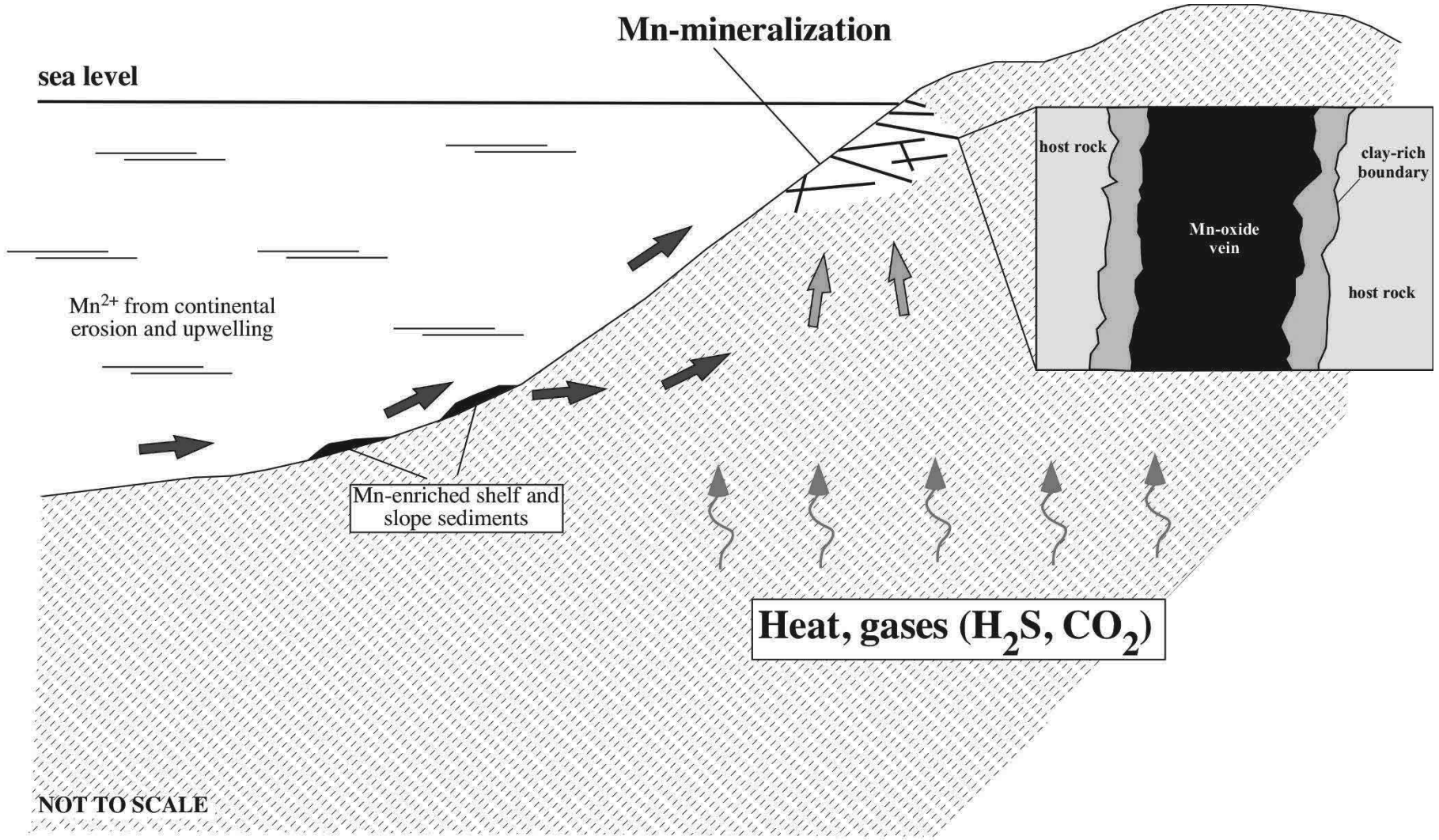
Mn-mineralization
sea level
host rock
clay-rich boundary
Mn-oxide vein
host rock
Mn^{2+} from continental erosion and upwelling
Mn-enriched shelf and slope sediments
Heat, gases (H_2S, CO_2)
NOT TO SCALE

Sampling site	La Piramide	La Piramide	La Piramide	La Piramide	Cala Fico	La Piramide	La Piramide	Cala Fico	Punta Senoglio	Ventrisco
Description	vein	vein	nodule	ocelli	vein	host rock (bulk ignimbrite)	host rock (bulk ignimbrite)	host rock (lava)	UCI (unaltered juvenile fraction)	UCI (unaltered juvenile fraction)
Sample	QM-2v	QM-8v	QM-14v	QM-9o	QM-6v	QM-8	QM-9	SP-72	SP-66	SP-104
SiO_2 wt%	27.76	15.38	30.03	74.05	42.55	74.24	73.10	74.84	74.39	72.28
TiO_2	0.06	0.03	0.10	0.19	0.06	0.24	0.24	0.17	0.27	0.25
Al_2O_3	3.71	2.84	5.78	10.81	6.31	11.67	12.53	12.26	11.57	9.93
Fe_2O_{3T}	2.61	1.25	1.16	3.33	2.38	4.08	4.01	3.23	3.83	5.44
MnO	50.93	64.83	48.49	1.96	36.37	0.06	0.05	0.06	0.06	0.12
MgO	0.35	0.37	0.24	bdl	bdl	0.07	0.02	0.09	0.04	0,10
CaO	0.25	0.12	0.25	bdl	bdl	0.09	0.07	0.14	0.08	0.19
Na_2O	1.78	1.08	1.78	3.45	2.38	3.98	3.86	4.62	4.54	3.80
K_2O	3.61	2.87	4.14	4.38	4.54	4.44	4.39	4.59	4.52	4.03
P_2O_5	0.10	0.10	0.14	bdl	0.04	0.02	0.05	bdl	0.04	bdl
L.O.I.	8.84	11.13	7.89	1.83	5.37	1.11	1.68	0.99	0.66	3.85
Mn/Fe	21.78	57.88	46.65	0.66	17.05	0.02	0.01	0.02	0.02	0.02
$([K_2O]+[Na_2O])/[Al_2O_3]$	1.84	1.72	1.28	0.96	1.40	0.97	0.89	1.02	1.07	0.61
Li ppm	9.6	10.7	11.7	41	32.2	56	40	46	15.4	81
Be	62	55	53	6.9	43	7.1	5.6	7.2	6.3	12.6
Sc	2	3	2	7	4	6	6	5.1	5	5
V	15	12	15	6	7	1	1	<1	2	0.2
Cr	< 1	< 1	< 1	< 1	< 1	< 1	< 1	1.12	2	bdl
Co	7	11	3	< 1	70	< 1	< 1	<1	0.5	0.3
Ni	24	29	3	1	23	< 1	< 1	<1	1	1
Cu	2	3	2	1	92	< 1	< 1	-	-	-
Zn	627	639	513	117	1309	131	92	-	-	-
Ga	15.6	15.8	19.0	30.6	30.2	28.8	23.5	-	-	-
Rb	101	69	71	234	197	276	206	283	201	326
Sr	1652	2307	2666	21.5	552	9.6	5.9	3.07	15.7	5.6
Y	137	297	33.3	180	300	48	74	120	96	204
Zr	412	358	185	1539	278	1042	919	839	793	1695
Nb	52	32.5	55	167	111	131	98	112	105	192
Mo	9.8	1.30	19.9	15.8	126	0.78	0.43	0.68	2.2	9.4
Cs	1.38	5.1	4.5	0.74	3.29	0.93	0.62	4.2	2.96	11.3
Ba	8773	18094	2995	779	2121	15.2	13.9	6.5	63	14
La	230	415	41	326	678	37	113	98	125	206
Ce	266	708	172	1053	2185	115	261	196	220	410
Pr	43	97	7.9	75	152	8.6	26.2	24.1	28.8	47
Nd	156	350	28.1	257	550	29.1	90	88.9	110	170
Sm	30.6	71	5.9	48	158	5.6	16.7	19.5	22.7	35
Eu	1.49	2.82	0.49	1.23	1.14	0.18	0.42	0.10	0.97	0,91
Gd	29.0	65	5.9	36	143	5.2	12.6	16.9	18.3	29.5
Tb	4.5	10.4	0.97	5.9	19.2	0.99	2.21	2.90	3.1	5.1
Dy	24.3	58	5.6	34	81	6.9	14.0	18.9	18.4	33
Ho	4.5	11.3	1.13	6.7	12.5	1.56	2.73	3.95	3.7	7.1
Er	11.3	30.0	3.08	19.2	26.0	5.1	8.1	11.2	9.9	19.7
Tm	1.50	4.0	0.43	2.95	2.94	0.90	1.29	1.80	1.57	3.1
Yb	8.6	22.3	2.55	19.1	15.6	6.3	8.5	10.7	9.2	17.9
Lu	1.23	3.25	0.38	2.76	2.02	1.09	1.28	1.54	1.32	2.65
Hf	9.9	7.9	3.9	29.0	7.8	23.8	20.2	22.8	20.1	41
Ta	2.58	1.79	1.93	8.8	4.9	8.8	7.1	8.0	7.1	13.6
W	0.31	0.26	0.39	4.3	10.3	1.18	0.86	0.49	1.66	1.49
Pb	6.1	21.0	2.17	218	173	11.3	18.7	64	56	67
Th	12.6	11.8	3.3	55	21.3	34	34	35	23.8	50
U	11.0	22.1	5.8	6.2	20.4	2.33	2.62	5.2	6.4	13.3
ΣREE ppm	812	1847	276	1887	4026	224	558	495	573	987
Ce_N/Ce_N*	0.56	0.77	2.04	1.47	1.48	1.40	1.05	0.89	0.86	0.97
Eu_N/Eu_N*	0.17	0.14	0.28	0.10	0.03	0.11	0.10	0.02	0.12	0.10
$^{206}Pb/^{204}Pb$	18.9943 ±0.0007	18.9271 ±0.0004	-	-	18.7488 ±0.0006	-	-	-		
$^{207}Pb/^{204}Pb$	15.6659 ±0.0007	15.6685 ±0.0003	-	-	15.6648 ±0.0006	-	-	-		
$^{208}Pb/^{204}Pb$	38.9613 ±0.0019	38.9284 ±0.0008	-	-	38.7789 ±0.0017	-	-	-		

Table 1. Geochemical analyses of Mn ores and of host rock at La Piramide and Cala Fico sites and of the unaltered juvenile fraction of UCI. Fe_2O_{3T}: all Fe as Fe_2O_3 wt%; L.O.I.: Loss on Ignition; bdl: below detection limit; -: not analysed; Ce and Eu anomalies calculated with chondrite-normalized values (normalization values from McDonough and Sun, 1989). Pb isotope ratios: errors quoted are within run; the external reproducibility is between ± 0.016 and ±0.018% (2 S.D.) for all ratios.

Sampling site	La Piramide	La Piramide	La Piramide	La Piramide	La Piramide	Cala Fico	La Piramide	La Piramide
Sample	QM-8v	QM-8v	QM-8v	QM-2v	QM-2v	QM-6v	QM-8v	QM-2v
Phase	Cry	Cry	Cry-Hol	Hol	Cry-Hol	Mn + Ce	Mnz(Ce)	Mnz(La)
SiO_2	0.61	0.30	4.58	19.34	0.44	10.60	3.09	-
Al_2O_3	0.33	-	2.71	5.53	0.64	1.91	-	0.44
FeO_{TOT}	0.19	0.20	2.65	1.41	0.82	0.34	1.02	-
MnO	91.27	92.24	80.75	61.28	90.8	41.66	4.31	19.99
MgO	0.48	0.56	0.74	1.03	0.38	0.99	-	0.26
CaO	0.27	0.13	0.36	0.41	-	1.08	-	6.08
Na_2O	0.79	0.61	0.62	2.62	0.33	-	1	-
K_2O	5.2	5.45	3.9	2.60	3.27	1.21	0.65	1.03
ClO	-	-	-	-	-	1.78	-	-
SO_3	-	-	-	-	-	-	-	0.26
BaO	0.86	0.39	3.68	5.78	3.31	-	0.66	-
ZnO	-	0.12	-	-	-	-	-	-
P_2O_5	-	-	-	-	-	2.03	30.51	32.04
La_2O_3	-	-	-	-	-	-	22.28	23.96
Ce_2O_3	-	-	-	-	-	38.25	29.84	0.49
Nd_2O_3	-	-	-	-	-	-	6.63	15.45
TOT.	100	100	99.99	100	99.99	99.85	99.99	100

Sampling site	La Piramide	La Piramide	La Piramide	La Piramide	La Piramide	La Piramide
Sample	QM-8v	QM-8v	QM-8v	QM-2v	QM-2v	QM-2v
Phase	Sm	Sm	Sm	Sm	Sm	Sm
SiO_2	55.91	53.82	55.02	55.64	55.60	55.30
TiO_2	-	-	0.71	0.93	0.92	0.68
Al_2O_3	7.60	6.92	6.34	27.92	27.84	27.47
FeO_{TOT}	30.51	34.47	27.75	10.96	10.64	10.78
MnO	0.48	0.35	0.74	1.03	0.76	1.20
MgO	1.56	1.44	4.66	1.46	1.52	1.23
CaO	2.28	2.44	2.80	1.32	1.44	1.62
Na_2O	0.30	0.12	1.07	0.27	0.45	0.25
K_2O	1.36	0.44	0.91	0.77	0.83	1.47
TOT.	100	100	100	100	100	100
Si	7.83	7.68	7.67	6.96	6.94	6.95
Ti	-	-	0.07	0.09	0.09	0.06
Al	1.25	1.16	1.04	4.07	4.10	4.07
Fe^2	3.57	4.11	3.24	1.15	1.11	1.13
Mn	0.06	0.04	0.09	0.11	0.08	0.13
Mg	0.33	0.31	0.97	0.27	0.28	0.23
Ca	0.34	0.37	0.42	0.18	0.19	0.22
Na	0.08	0.03	0.29	0.07	0.11	0.06
K	0.24	0.08	0.16	0.12	0.13	0.24

Table 2. EDS analysis of Mn ores and alteration mineral in representative samples of La Piramide and Cala Fico sites. Smectite formulas calculated based on 22 oxygens. Cry = Cryptomelane; Hol = Hollandite; Mnz = Monazite; Sm = Smectite; - : not analysed.